# Dissecting intratumor heterogeneity of nodal B cell lymphomas on the transcriptional, genetic, and drug response level

Tobias Roider[1-3], Julian Seufert[4-5], Alexey Uvarovskii[6], Felix Frauhammer[6], Marie Bordas[4,7], Nima Abedpour[8], Marta Stolarczyk[1], Jan-Philipp Mallm[9], Sophie Rabe[1-3,5,10], Peter-Martin Bruch[1-3], Hyatt Balke-Want[11], Michael Hundemer[1], Karsten Rippe[9], Benjamin Goeppert[12], Martina Seiffert[7], Benedikt Brors[13], Gunhild Mechtersheimer[12], Thorsten Zenz[14], Martin Peifer[8], Björn Chapuy[15], Matthias Schlesner[4], Carsten Müller-Tidow[1-3], Stefan Fröhling[10,16], Wolfgang Huber[2,3], Simon Anders[6*], Sascha Dietrich[1-3,10*]

[1] Department of Medicine V, Hematology, Oncology and Rheumatology, University of Heidelberg, Heidelberg, Germany,
[2] Molecular Medicine Partnership Unit (MMPU), Heidelberg, Germany,
[3] European Molecular Biology Laboratory (EMBL), Heidelberg, Germany,
[4] Bioinformatics and Omics Data Analytics, German Cancer Research Center (DKFZ), Heidelberg, Germany,
[5] Faculty of Biosciences, University of Heidelberg, Heidelberg, Germany,
[6] Center for Molecular Biology of the University of Heidelberg (ZMBH), Heidelberg, Germany,
[7] Division of Molecular Genetics, German Cancer Research Center (DKFZ), Heidelberg, Germany,
[8] Department for Translational Genomics, University of Cologne, Cologne, Germany,
[9] Division of Chromatin Networks, German Cancer Research Center (DKFZ) & Bioquant, Heidelberg, Germany,
[10] Department of Translational Medical Oncology, National Center for Tumor Diseases (NCT) Heidelberg and German Cancer Research Center (DKFZ), Heidelberg, Germany,
[11] Department I of Internal Medicine, University Hospital of Cologne, Cologne, Germany,
[12] Institute of Pathology, University of Heidelberg, Heidelberg, Germany,
[13] Division of Applied Bioinformatics, German Cancer Research Center (DKFZ), Heidelberg, Germany,
[14] Department of Medical Oncology and Hematology, University of Zürich, Zürich, Switzerland,
[15] Clinic for Hematology and Medical Oncology, University Medicine Göttingen, Göttingen, Germany,
[16] German Cancer Consortium (DKTK), Heidelberg, Germany.

* *These authors contributed equally.*

**Corresponding Author**

Sascha Dietrich, MD PhD
Email address: sascha.dietrich@embl.de
Mailing address: Department of Medicine V, University Hospital Heidelberg
Im Neuenheimer Feld 410
69120 Heidelberg, Germany
Phone: +49 6221 56 39894

39 Fax: +49 6221 56 4049

## Contributions

T.R., M.B., M.St., JP.M., S.R. and PM. B. performed experiments. T.R., J.S., A.U., F.F., M.B., N.A., H.BW., M.P., M.Sc. and S.A. analyzed the data. T.R., M.H., K.R., B.G., M.Se., B.B., G.M., C.MT., S.F., W.H., S.A. and S.D. interpreted the data. T.R., T.Z., S.F. and S.D. designed the study. T.R., J.S., K.R., B.C., M.Sc., W.H., S.A. and S.D wrote the paper

## Acknowledgements

T.R. was supported by a physician scientist fellowship of the Medical Faculty of University Heidelberg. M.Se. was supported by a grant of the Deutsche Forschungsgemeinschaft (DFG). S.D. was supported by a grant of the Hairy Cell Leukemia Foundation, the Heidelberg Research Centre for Molecular Medicine (HRCMM) and an e:med BMBF junior group grant. For the data management we thank the Scientific Data Storage Heidelberg (SDS@hd) which is funded by the state of Baden-Württemberg and a DFG grant (INST 35/1314-1 FUGG). We thank Carolin Kolb (University Hospital Heidelberg) and Mareike Knoll (German Cancer Research Center Heidelberg) for their excellent technical assistance. We also thank the DKFZ Single-Cell Open Lab (scOpenLab) for the experimental assistance in terms of scRNA-seq. Also, this study was supported by the Heidelberg Center for Personalized Oncology (DKFZ-HIPO). We thank the DKFZ Omics IT and Data Management Core Facility (ODCF) and the DKFZ Genomics and Proteomics Core Facility (GPCF) for their technical support.

**Abstract**

Tumor heterogeneity encompasses both the malignant cells and their microenvironment. While heterogeneity between individual patients is well-known to affect the efficacy of anti-cancer drugs, most personalized treatment approaches do not account for intratumor heterogeneity. We addressed this issue by studying the heterogeneity of lymph node-derived B cell non-Hodgkin lymphoma (B-NHL) by single cell RNA-sequencing (scRNA-seq) and transcriptome-informed flow cytometry. We identified transcriptionally distinct malignant subclones and compared their drug response and genomic profiles. Malignant subclones of the same patient responded strikingly different to anti-cancer drugs ex vivo, which recapitulated subclone-specific drug sensitivity during in vivo treatment. Tumor infiltrating T cells represented the majority of non-malignant cells, whose gene expression signatures were similar across all donors, whereas the frequencies of T cell subsets varied significantly between the donors. Our data provide new insights into the heterogeneity of B-NHL and highlight the relevance of intratumor heterogeneity for personalized cancer therapies.

## Introduction

The genomic and transcriptional landscape of many cancer entities has been catalogued over recent years, documenting the range of tumor heterogeneity between individual patients [1]. In addition, it has long been appreciated that tumors within each patient consist of diverse, but phylogenetically-related subclones [2]. Bulk sequencing studies of tumor cells have been conducted to infer the genetic spectrum of intratumor heterogeneity from variant allele frequencies of somatic mutations [3]. While important insights were gained from these studies, further characterization on the single cell level is needed to more accurately dissect the pathway and molecular properties associated with distinct subclones.

Neoplastic cells alone do not manifest a malignant disease, but attract a battery of non-malignant bystander cells, which support tumor cell growth and survival. The diversity and plasticity of the microenvironment constitutes another layer of heterogeneity, beyond the heterogeneity of the cancer cells themselves [4]. There is solid evidence that intratumor heterogeneity among malignant and non-malignant cells, and their interactions within the tumor microenvironment are critical to diverse aspects of tumor biology, response to treatment, and prognosis [5].

While bulk genomic tissue profiling has only a limited ability to reconstruct the complex cellular composition of tumors, single cell DNA-sequencing [6, 7] and RNA-sequencing (scRNA-seq) methods [8-11] have emerged as powerful tools to study intratumor heterogeneity and reconstruct the full picture of malignant and non-malignant cells. These technologies further enable researchers to identify rare cell types such as cancer stem cells [12] and circulating tumor cells [13, 14], or to follow clonal dynamics during cancer treatment [15]. Most of these single cell studies have been used to describe distinct cell subpopulations on the transcriptional level, but their functional properties, such as drug response profiles, remain largely unexplored.

To address this, we used B cell non-Hodgkin lymphoma (B-NHL) as a model disease entity to dissect intratumor heterogeneity on the transcriptional, genetic, and functional (drug response) level. In parallel, we investigated the cellular heterogeneity of the B-NHL lymph node microenvironment. B-NHL are a heterogenous group of hematologic malignancies that most frequently grow in the lymph node compartment. Almost half of all B-NHL are classified as diffuse large B cell lymphoma (DLBCL) or follicular lymphoma (FL) [16]. Transformation of indolent FL into aggressive DLBCL is observed in approximately 10% of all FL cases [17]. Despite effective treatment options, 20-40% of B-NHL patients relapse multiple times and present with chemotherapy refractory disease [18, 19]. The response to single agent targeted

therapy in these patient cohorts is surprisingly low [20, 21]. Intratumor heterogeneity might be a key factor contributing to therapeutic failure and low success rate of these single agent targeted therapies [3]. Understanding subclonal drug response patterns would therefore be an important asset for designing more effective personalized lymphoma therapies.

To dissect the complex cellular composition of the malignant lymph node niche, we profiled transcriptomes of malignant and non-malignant cells derived from 12 different reactive or B-NHL lymph node biopsies. We further studied the variation of the cellular composition of the malignant lymph node niche by flow cytometry in a larger cohort of 41 patients. Among malignant cells, we identified transcriptionally distinct malignant subclones and characterized these subclones further by ex-vivo drug perturbation and genome sequencing. This revealed new insights into intratumor heterogeneity of B-NHL and demonstrated substantially different drug responses between malignant subclones in the same patient.

## Results

### *Study outline*

We designed an experimental pipeline to dissect the heterogeneity of non-malignant and malignant lymph node-derived lymphocytes (Figure 1A). This involved first preparing single cell suspensions of B-NHL lymph node biopsies and performing scRNA-seq. These single cell transcriptomic data were then used to identify transcriptionally-distinct subclones by flow cytometry using distinguishing subclone-specific surface markers, and finally the subclones were functionally interrogated in drug perturbation assays with a comprehensive panel of 58 drugs in five concentrations, and further characterized by whole genome (WGS) and/or exome sequencing (WES).

### *Dissecting the cellular composition of nodal B cell lymphomas*

We assayed single cell suspensions of a total of 12 samples: four germinal center-derived diffuse large B cell lymphoma (DLBCL) samples, of which two were transformed from FL (DLBCL1, DLBCL2, tFL1, tFL2), one non-germinal center-derived DLBCL (DLBCL3), four follicular lymphoma samples (FL1, FL2, FL3, FL4), and three reactive non-malignant lymph node sample (rLN1, rLN2, rLN3) by flow cytometry and droplet-based scRNA-seq (Supplementary Table 1). After removal of low-quality cells, we analyzed scRNA-seq profiles of 13,259 malignant and 9,296 non-malignant cells with an average sequencing depth of 1,409 genes per cell.

First, we verified that the lymph node-derived single cell suspensions were representative for the cellular composition (B and T cells) of the lymphoma and its microenvironment in vivo. We used sections of paraffin-embedded samples of the same lymph nodes, which were formalin fixed directly after surgical excision and therefore represent the in vivo cellular composition, and quantified B and T cell frequencies by immunohistochemistry (IHC, Supplementary Figure 1A). In parallel, we calculated B and T cell frequencies by flow cytometry and scRNA-seq in single cell suspensions (Supplementary Figure 1A, B). The frequencies of B and T cells derived from scRNA-seq correlated very well with the frequencies determined by flow cytometry ($r = 0.97$, $n = 12$, Figure 1B) and IHC ($r = 0.92$, $n = 7$, Figure 1C).

Next, we aimed to distinguish malignant from non-malignant B cells and delineate these populations in our single cell experiments. We took advantage of the fact that malignant B cell populations express only one type of immunoglobulin light chain (LC), either κ or λ [22]. We calculated the LC-ratio (κ/λ) based on RNA expression of the genes *IGKC* (coding for the constant part of the κ LC) and *IGLC2* (λ LC) for each single B cell and color-coded this ratio

in a t-distributed stochastic neighbor embedding (t-SNE) plot (Figure 1D, E). In the malignant lymph nodes, we could either identify both a non-malignant and malignant or only malignant B cell clusters (Supplementary Figure 2). In contrast, reactive lymph node samples contained only non-malignant B cells (see method section for details).

We further evaluated the frequencies of these subsets in a larger cohort of 41 lymph node samples by flow cytometry, including those samples used for scRNA-seq. Both approaches showed very similar frequencies of these cell subsets ($r = 0.97$, $n = 12$, Supplementary Figure 3A, B). We found that the proportion of malignant cells was highly variable across samples. It ranged from 14.6 to 97.2 % (median 79.3 %, $n = 9$) in DLBCL, 23.7 to 85.4 % (median 79.9 %, $n = 12$) in FL, 48.4 to 95.5 % (median 88.0 %, $n = 4$) in mantle cell lymphoma, and 65.4 to 91.4 % (median 83.1 %, $n = 7$) in chronic lymphocytic leukemia (Supplementary Figure 3C). This substantial cellular heterogeneity complicates bulk sequencing approaches of unsorted lymph node samples, and highlights the value of single cell sequencing to simultaneously study the full spectrum of malignant and non-malignant lymph node cells.

***Characterization of lymph node-derived T cell populations***

T cells are key players of the host-specific tumor immunosurveillance [23]. B-NHL exhibit genetic immune escape strategies that can be targeted using current therapeutic strategies [24], including checkpoint inhibitors [25] and bispecific antibodies [26]. Notably, lymphoma cells can also orchestrate their tumor microenvironment so that certain T cell subsets support the growth and proliferation of the tumor cells [27]. Even though these subsets have been extensively studied by immunophenotyping, their transcriptional heterogeneity in B-NHL lymph nodes, in particular at the single cell level, still remains to be elucidated.

We combined single cell RNA expression profiles of T cells from all 12 donors and jointly visualized them by Uniform Manifold Approximation and Projection (UMAP), a dimension reduction algorithm alternative to t-SNE [28]. Many well-established surface markers, which are used to distinguish T cell subsets in flow cytometry studies, are insufficiently expressed on the scRNA-seq level. We therefore chose unsupervised clustering to partition T cells into transcriptionally distinct subsets, which were then annotated by differentially expressed marker genes. All T cells from either reactive or malignant lymph nodes distributed to only four major T cell subpopulations (Figure 2 A, B). Note, that clusters were not driven by patients or disease entity, suggesting only limited transcriptional heterogeneity across all donors. Apart from conventional T helper cells ($T_H$; *CD4, IL7R, PLAC8, KLF2*) and regulatory T cells ($T_{REG}$; *CD4,*

188 *IL2RA, FOXP3, ICOS*), we identified a third T helper cell population, which was characterized
189 by overexpression of *PDCD1* (PD1)*, ICOS, CXCR5, TOX, TOX2* and *CD200* (Figure 2C,
190 Supplementary Table 2), suggesting a T follicular helper cell ($T_{FH}$) phenotype [29-33]. In
191 contrast to the diversity of T helper cells, we observed only one major cluster of cytotoxic T
192 cells ($T_{TOX}$, *GZMK*, *CCL4/5*, *GZMA*, *NKG7*, *CD8A*). However, the frequencies of the four
193 identified T cell subsets were highly variable between different B-NHL donors (Figure 2D).
194 To study this variation in a larger cohort, we quantified the abovementioned T cell populations
195 in 39 lymph node samples of DLBCL, FL, mantle cell lymphoma and chronic lymphocytic
196 leukemia by flow cytometry using the most distinctive markers (CD3, CD4, CD8, CD25,
197 FoxP3, ICOS, PD1), as seen in Figure 2C. The frequencies of all T cell subsets derived from
198 scRNA-seq correlated well with the frequencies determined by flow cytometry ($r = 0.69$,
199 $n = 10$, Figure 2E). We found that $T_{FH}$ cells were significantly increased in FL (two-sided
200 Wilcoxon test: $p = 0.006$, Figure 2F), and $T_{REG}$ cell frequencies were significantly increased in
201 malignant lymph nodes, compared to the reactive ones (two-sided Wilcoxon test: p values as
202 indicated, Figure 2F).
203 Taken together, we demonstrated that T cells derived from malignant B-NHL lymph nodes are
204 transcriptionally similar to those derived from non-malignant reactive lymph nodes. In contrast,
205 the proportion of individual T cell subsets differed significantly between lymphoma entities and
206 individual patients. This finding indicates that B-NHL shape their microenvironment by
207 influencing the recruitment of certain T cell subpopulations, but have less effect on their
208 transcriptional programs. Therefore, studying the frequencies of lymphoma infiltrating T cell
209 subsets and their effect on the outcome after immunotherapies might be highly relevant for the
210 development of biomarkers.
211
212 ***Identification of gene expression signatures driving B cell heterogeneity by scRNA-seq***
213 Next, we examined the heterogeneity of the malignant and non-malignant B cells. To gain a
214 global overview of the gene expression pattern across all malignant and non-malignant B cells
215 from the 12 different donors, we combined their single cell RNA expression profiles, clustered
216 them jointly and visualized them by UMAP (Figure 3A, B).
217 Clustering partitioned the non-malignant B cells into two distinct subpopulations (C0-C1,
218 Figure 3A). Among multiple differentially expressed genes between these two subsets
219 (Supplementary Table 3), we found *IGHM* and *CD72* to be overexpressed in cluster C0, which
220 characterizes naïve B cells [34], and *CD27* and *IGHG1* to be overexpressed in cluster C1, which
221 characterizes memory B cells [35].

Of the eight transcriptionally distinct clusters formed by the malignant B cells (C2-C9, Figure 3A), six exclusively contained cells of only one donor (Figure 3A, B). This suggests a higher degree of inter-patient heterogeneity for malignant than for non-malignant B cells. We performed a gene set enrichment analysis (GSEA) on the mean expression differences between each malignant B cell cluster and all non-malignant cells, which revealed multiple cluster-specific gene sets (Figure 3C). Germinal center (GC)-associated gene expression signatures were significantly enriched in all clusters except for cluster 6, which exclusively contained malignant B cells of DLBCL3. This finding supports the classification of all B-NHL cells as either GCB type DLBCL or FL, except for the remaining DLBCL3 sample, which was classified as a non-GCB type DLBCL based on the Hans-classifier (Supplementary Table 1) [36]. Individual clusters were characterized by oncogenic transcriptional programs, which indicated activation of oncogenic MYC or STK33 signaling (Figure 3D).

Inter-patient heterogeneity of B cell lymphomas also comprises their proliferative capacity, which can vary from very low in FL to very high in DLBCL. We determined the proportion of B cells in S, $G_2$ or M phase based on their single cell RNA profile (Supplementary Figure 4A) and observed a high correlation with flow cytometry- and IHC-based staining of Ki67 (R = 0.83 scRNA-seq to flow cytometry, R = 0.92, scRNA-seq to IHC, Supplementary Figure 4B).

In summary, these results indicate that inter-patient heterogeneity of malignant B cells, including their diverse proliferative activity, can be captured by the scRNA-Seq and can be linked to lymphoma-specific transcription signatures. Non-malignant B cells, however, had similar transcriptional profiles across different donors.

***Decoding the crosstalk between T cells and malignant B cells in the lymph node microenvironment***

Above, we concluded that B cell lymphomas shape their microenvironment by modulating the frequency of different subsets of lymphoma infiltrating T cells. We now aimed to understand through which potential ligand-receptor interactions malignant B cells could benefit from their specific T cell microenvironment. For this purpose, we adopted a computational approach described by Vento-Tormo et al. [37] and analyzed 760 known ligand-receptor combinations (Supplementary Table 4) to identify the most significant interactions between malignant B cells and lymphoma infiltrating T cells within the lymph node microenvironment (Figure 4A).

This analysis suggested that malignant B cells could receive costimulatory and coinhibitory signals by all four major T cell subsets, via CD80/CD86-CD28 and CD80/CD86-CTLA, while interactions via BCMA-BAFF, BAFF-R-BAFF and CD40-CD40LG could predominantly be

mediated by $T_H$ or $T_{REG}$ cells. Significant interaction scores of IL4-IL4R and IL4-IL13RA1 were exclusively observed between $T_{FH}$ and malignant B cells, providing further evidence that $T_{FH}$ cells represent the most important source of IL4 production in B cell lymphoma [38]. This observation might be of clinical relevance because the IL4/IL4R interaction is discussed as potential resistance mechanism against Bruton's tyrosine kinase (BTK) inhibitors [39, 40]. In line with the current state of knowledge [41-43], we also observed strong interaction scores for $T_{FH}$ via IL21-IL21R with malignant B cells and via IL2-IL2R with other T cell subsets. This analysis supports the classification of $T_{FH}$ cell as one of the four main T cell subsets within the lymph node microenvironment and reveals that each subset may provide a distinct panel of stimuli to interact with malignant B cells.

***Dissecting transcriptional intratumor heterogeneity using multicolor flow cytometry***

Intratumor heterogeneity of nodal B cell lymphoma is a well-known phenomenon, however, most available studies infer intratumor heterogeneity from variant allele frequencies of genetic alterations corrected for purity, ploidy and multiplicity of local copy number [44, 45].

Here, we aimed to investigate the genomic, transcriptomic and functional (drug response) layers of intratumor heterogeneity from single cells. Unsupervised clustering of scRNA-seq profiles of malignant and non-malignant B cells revealed that all malignant samples were composed of at least two or more transcriptionally distinct subclusters (Supplementary Figure 5). We aimed to validate scRNA-based clusters at the cellular level to understand if this clustering represents biologically and clinically relevant differences. Therefore, we selected three samples (FL4, tFL1, DLBCL1) based on the availability of material for follow-up studies. We inferred differentially expressed surface markers from single cell expression profiles and first validated the distinction of scRNA-based clusters by flow cytometry. In a second step, we cultured lymph node derived lymphocytes with 58 different drugs in 5 concentrations (Supplementary Table 5) and stained them with specific antibody combinations to assess their drug response profiles by flow cytometry. In a third step, we sorted subpopulation and performed genome sequencing for each subclone (tFL1, DLBCL1).

***Verifying five transcriptionally distinct clusters in follicular lymphoma sample***

The FL4 sample was collected at initial diagnosis. Based on single cell gene expression profiling, we identified five different B cell subpopulations (Supplementary Figure 6A). We aimed to validate all five clusters (C1 to C5) at the cellular level by flow cytometry and hence, we stained the differentially expressed surface markers CD44, CD24, CD22, CD27, kappa and

lambda light chain (encoded by IGKC and IGLC2, Supplementary Figure 6B). Using the ratio of *IGKC* and *IGLC2* (see Methods for details), we found benign B cells in C1, lambda-restricted malignant B cells in C2, and malignant B cells with only marginal expression of *IGKC* and *IGLC2* in C3 to C5 (Supplementary Figure 6C). The pattern of light chain expression could be perfectly comprehended using flow cytometry (Supplementary Figure 6D), enabling us to differentiate C1 versus C2 versus C3, C4 and C5. Cluster C3 could then be recognized by a high expression of CD44 (Supplementary Figure 6D, 6E). To further distinguish C4 and C5 among the $CD44^{Low}$ cells, we combined CD22, CD27 and CD24 and detected a subpopulation with $CD22^{High}$, $CD27^{High}$ and $CD24^{Low}$, which corresponded to the expression pattern of cluster C5 (Supplementary Figure 6F). This approach allowed us to proof all five scRNA-based clusters by flow cytometry with comparable frequencies.

To assess subclone-specific drug response, we stained for kappa and lambda light chains and focused on the two major populations (C2 ≙ $lambda^+$, C3-C5 ≙ $kappa/lambda^-$). We did not observe differential responses for the majority of targeted drugs, but we found that only the $kappa/lambda^-$ cluster was sensitive to chemotherapeutics (Supplementary Figure 6G). Interestingly, this patient received doxorubicin-based immunochemotherapy as first line treatment after sample collection and achieved only a partial remission.

***The indolent and aggressive component of transformed follicular lymphoma exhibit a distinct transcriptional, genomic and drug response profile***

For the tFL1 sample, we detected three transcriptionally distinct clusters of B cells based on single cell RNA expression profiling (Figure 5A, B). Two clusters exclusively contained malignant B cells, and one cluster contained non-malignant B cells. We assessed the proliferative activity of both malignant populations based on their gene expression profiles, and observed that only one malignant cluster contained cells in S phase (Supplementary Figure 7A), with no cells in $G_2$ or M phase (Supplementary Figure 7B). This suggests that this cluster represents a proliferating, thus aggressive component of the transformed FL. We performed a GSEA on the mean expression differences between the two malignant clusters, which revealed that gene expression signatures associated with MYC, MTORC1, and the $G_2M$ transition [46] were significantly enriched in the presumptively aggressive malignant B cell subclone (Supplementary Figure 7D-F).

Among the genes differentially expressed between both subclones, we found *FCGR2B* (Figure 5A), which encodes a surface receptor protein (CD32B), to be exclusively expressed in the presumptively indolent subclone. Thus, we confirmed the existence of three B cell populations

by flow cytometry (Figure 5C, see Supplementary Figure 8A for complete gating strategy). CD10 was strongly positive in both malignant B cell populations ($CD32^{High}$, $CD32^{Low}$), but not in non-malignant B cells.

As described above, we measured the ex vivo drug responses separately for each subclone (Figure 5D, E) and observed very different drug response profiles for the two malignant subclones. The BTK inhibitors, ibrutinib, acalabrutinib, and tirabrutinib, and the immunomodulatory imide drugs (pomalidomide, lenalidomide), were exclusively active in the $CD32^{Low}$ subclone, whereas HDAC inhibitors (panobinostat, romidepsin, vorinostat) were more active in the $CD32^{High}$ subclone.

Based on CD32 and CD10 expression, we sorted the three B cell subclones by flow cytometry (Supplementary Figure 8A) and performed WES of peripheral blood-derived normal control DNA, whole tumor DNA, DNA of both malignant subclones, and DNA of the non-malignant B cell population. Copy number profiles of both malignant subclones were very different, including exclusive aberrations of chromosomes 3, 4, 6, 10, 12, 15, 18 and X (Supplementary Figure 7F). Only the $CD32^{Low}$ subclone harbored a trisomy 12 (Figure 5F), which was confirmed by scRNA-seq data (Figure 5G). Trisomy 12 has been associated with a better response to B cell receptor (BCR) signaling inhibitors [47], which was consistent with our observation that this subclone was more responsive to these drugs (Figure 5D, E). We also detected 157 somatic single nucleotide variants (SNV) in exonic regions, of which 25 (15.9 %) or 24 (15. 2%) were exclusively detected in the $CD32^{High}$ or $CD32^{Low}$ subclone, respectively (Figure 5H, I, Supplementary Table 6). However, the majority of somatic SNVs were equally represented in both subclones, indicating a phylogenetic relationship. We compared the allele count of all exonic SNVs between all three B cell populations and did not detect somatic SNV in healthy B cells (Figure 5J), which supports the validity of our sorting approach.

Taken together, scRNA-seq allowed us to identify different subclones within the same lymph node, which were genetically and functionally distinct in clinically-relevant aspects.

***A subclone-specific copy number variation of MYC drives a distinct gene expression and drug response program***

The DLBCL1 sample was collected from a patient with a chemotherapy refractory disease during progression, but before retreatment. Using scRNA-seq, we identified two distinct clusters of malignant B cells, which exhibited a high number of differentially expressed genes associated with diverse cellular programs (Figure 6A, B), such as BCR signaling (*PRKCB*, *NFKB1I*), cytokine signaling (*LGALS9*, *IFITM1*), MAPK signaling (*RGS13*, *FBLN5*) and

antigen processing (*PTPN22*, *SELL*, *CD48)*. Among the differentially expressed genes, we found *CD48* and *SELL* (Supplementary Figure 9A, B*)*, which encode for the surface markers CD48 and CD62L respectively. Staining for CD48 and CD62L by flow cytometry validated the existence of the two distinct subclones (Figure 6C). The proportions of both clusters ($CD48^{High}CD62L^{+}$, $CD48^{Low}CD62L^{-}$) calculated based on flow cytometry and scRNA-seq were comparable, indicating good concordance between RNA and protein expression. We measured again the ex vivo drug responses for each subclone (Figure 6D, E) and observed a strikingly different drug response profile between the two subclones: B cell receptor (BCR) signaling inhibitors (acalabrutinib, tirabrutinib, ibutinib, duvelisib, idelalisib, entospletinib) and CDK inhibitors were exclusively effective in the $CD48^{Low}CD62L^{-}$ subclone, whereas Bromodomain and Extra-Terminal motif (BET) inhibitors (I-BET-762, OTX015), nucleoside analogues (cytarabine, fludarabine, cladribine) and vincristine were exclusively efficacious in the $CD48^{High}CD62L^{+}$ subclone.

We sorted viable tumor cells based on surface markers (CD48, CD62L, Supplementary Figure 8B) and performed WGS on each subclone separately, as well as on the whole tumor sample. In total, we detected 240 non-synonymous SNV located in exonic regions (Supplementary Table 7), however, only 1 (0.4 %) or 5 (2.1 %) SNV were exclusively detected in the $CD48^{Low}CD62L^{-}$ or the $CD48^{High}CD62L^{+}$ cluster, respectively (Figure 6F). We further compared CNV profiles of the two subclones and detected a number of differences: the $CD48^{High}CD62L^{+}$ cluster carried an additional copy of *MYC* (8q24, Figure 6G), which was reflected by increased *MYC* expression levels (Supplementary Figure 9C). The q arm of chromosome 14 harbored two copy number gains and one copy number loss in the $CD48^{High}CD62L^{+}$ cluster (Figure 6G). Moreover, chromosome X exhibited a copy number gain of the p arm in the $CD48^{High}CD62L^{+}$ cluster, and a copy number loss of the q arm in the $CD48^{Low}CD62L^{-}$ cluster (Figure 6G).

Since pathologic activation of MYC renders cells sensitive to BET inhibitors [48, 49], we performed intracellular flow cytometry-based staining of MYC at baseline and after 24 hours incubation with and without the two BET inhibitors, I-BET-762 or OTX015. We confirmed the increased MYC expression level of the $CD48^{High}CD62L^{+}$ subclone at baseline (Figure 6H, Supplementary Figure 9D), and, as expected, found that MYC was downregulated upon incubation with I-BET-762 and OTX015, but not upon incubation with the BTK inhibitor ibrutinib (Figure 6H, Supplementary Figure 9E-G).

***In vivo retreatment confirms ex vivo prediction of subpopulation-specific drug response***

To exemplify the translational relevance of subclone-specific drug responses, we performed WES of DLBCL1 during the second relapse after retreatment with high-dose cytarabine. Based on ex vivo drug perturbation we had predicted that the $CD48^{High}CD62L^{+}$ but not the $CD48^{Low}CD62L^{-}$ subpopulation would respond to cytarabine (Figure 6D). We compared several synonymous SNV exclusive to the $CD48^{High}CD62L^{+}$ subpopulation before retreatment and during second relapse, and observed that the cytarabine-sensitive subpopulation was successfully eradicated (Figure 6I). Due to the lack of sufficiently exclusive SNV in the resistant subclone, we took advantage of the loss of heterozygosity (LOH) on chromosome Xq (Figure 6G) to determine the aberrant fraction of cells harboring a loss of Xq before and after retreatment. We found that the fraction of chemotherapy-resistant cells, harboring the loss of Xq, increased from 72 % to 93 % (see methods section for details).

In summary, we dissected the intratumor heterogeneity of the DLBCL1 sample on the transcriptional, genomic, and drug response level. This clinically relevant example highlights the huge translational relevance of tumor subpopulations and their specific drug response profile for personalized cancer treatment.

## Discussion

Intratumor heterogeneity poses a significant challenge for the clinical management of cancer patients. Advances of single cell technologies facilitated the profiling of intratumor heterogeneity at an unprecedented resolution [50]. Most of these studies comprehensively describe intratumor heterogeneity on the transcriptional level, but do not explore its functional consequences such as response or resistance to drugs. In this study, we address this limitation and identify transcriptionally distinct malignant subclones in B-NHL lymph node biopsies. We study differential drug response patterns of these subclones and genetic events which likely drove these differences.

Our analysis revealed the coexistence of up to four transcriptionally distinct subpopulations of malignant cells within individual B-NHL lymph node samples. This result recapitulates similar observations in follicular lymphoma [45], multiple myeloma [51] and other cancer entities [8, 12, 52]. We and others attributed this heterogeneity to differentially enriched gene sets, which indicate, for instance, activity of *MYC*, proliferation, or germinal center experience. However, we went further and established a straightforward strategy to prove the coexistence of up to four different tumor subpopulations at the cellular level. We subsequently performed perturbation assays with a comprehensive panel of clinically relevant drugs and observed that tumor subclones within the same lymph node responded strikingly different both to targeted compounds, such as ibrutinib, but also chemotherapeutics. The study by de Boer and colleagues supports our observation by demonstrating that acute myeloid leukemia subclones, which were identified on the basis of 50 leukemia-enriched plasma membrane proteins, had distinct functional properties including a differential sensitivity to FLT3-inhibition driven by a subclonal FLT3-ITD mutation [53]. Most preclinical in vitro and in vivo drug screens do not address such clonal heterogeneity, which may explain the failure of numerous drug candidates in the clinic [47]. For a single patient, we even demonstrated that the ex vivo drug response profiling correctly predicted the treatment sensitivity of tumor subclones in vivo. The prospective identification of rational combinations of cancer drugs that effectively target co-existing tumor subclones separately could avoid the outgrowth of resistant tumor clones under therapeutic pressure of a single drug, and would thereby improve efficacy of cancer treatments. Our study addresses this limitation of many ex vivo drug perturbation studies, and, due to its unbiased approach to prospectively dissect the malignant substructure, it is also generalizable to other cancer entities. However, due to the limitation of lymph node derived primary cells, we have to acknowledge that we could not apply our approach to all samples. Further studies

are necessary to expand this approach and to address also spatial heterogeneity of malignant tumors.

Our approach enabled us to directly identify genetic factors that underlie the transcriptional and drug response differences between subclones. This distinguishes our work from a previous scRNA-seq study in FL, which indirectly compared allele frequencies of bulk WES with the size of transcriptionally distinct subclones [45]. The authors found a correlation between genomic alterations and subclonal fractions and concluded that somatic mutations are associated with transcriptional differences. These findings are in contrast to another study, which correlated subclusters derived from targeted single cell expression profiling of 91 genes with subclusters derived from single cell immunoglobulin heavy-chain (IGH) sequencing. In this study, the authors concluded that distinct gene expression clusters were not associated with subclones derived from IGH hypermutations [54]. While these studies provide only indirect evidence, we physically sorted tumor subclones and normal B cells, and performed WGS or WES separately for transcriptionally distinct lymphoma subpopulations. With regard to somatic mutations, we observed two different scenarios: in the DLBCL1 sample we identified almost no somatic SNVs to be exclusive for one or the other subclone, whereas in the tFL1 sample we found up to 15% exclusive somatic SNVs in each subclone. However, both examples represent scenarios where subclone specific drug profiles could not have been predicted by means of gene mutation sequencing. We further compared CNV profiles of the same tumor subclones, and found that all subclones harbored significantly different CNV profiles, suggesting that copy number alterations represent an important layer of genetic events which can drive differential gene expression programs and drug response profiles. Although our results support the general notion that genetic events drive subclone specific differences in drug response, they also highlight the difficulty to predict drug responses based on only genome sequencing in clinical practice. It might therefore be beneficial to obtain both genetic- and drug response profiles for personalized treatment decisions.

Exploring the heterogeneity of the immune microenvironment in B-NHL has the potential to better reveal how lymphomas shape their microenvironment and how lymphoma patients could be better stratified for the treatment with immunotherapies. T cells represented the largest non-malignant population in B NHL lymph node biopsies. We identified four major, transcriptionally distinct T cell subpopulations, which were annotated as cytotoxic T cells, regulatory T helper cells, conventional T helper cells and T follicular helper cells [29-33]. We measured the frequency of these T cell subsets in an extended cohort of malignant lymph node biopsies and found T follicular helper cells to be enriched in FL, which is in line with previous

flow cytometry-based studies [33, 55]. These T cell subsets displayed only limited transcriptional heterogeneity with less variability between lymph nodes compared to malignant cells. However, the frequencies of these T cell subsets varied significantly across donors, which suggests that B-NHL shape their microenvironment by regulating the recruitment of different T cell subsets. This observation might be of clinical relevance, because cold tumors with very few infiltrating T cells have been reported to respond less well to immunotherapies [56].

Despite the rather small number of analyzed B-NHL patients, our study is of high clinical relevance. We demonstrated that the prospective identification of pre-existing transcriptionally distinct malignant subclones might be of diagnostic value to detect difficult to treat tumor subclones. In addition, our research establishes scRNA-seq as a new key technology for precise molecular profiling of relapsed and refractory nodal B cell lymphomas, and facilitates the design of new and molecularly-informed diagnosis and treatment strategies.

## Online Methods

*Patients samples and lymph node procession*

Our study was approved by the Ethics Committee of the University of Heidelberg. Informed consent was obtained in advance. Immediately after the excision, the lymph node was cut in small pieces and put into Roswell Park Memorial Institute (Gibco) medium supplemented with 10 % fetal bovine serum (FBS, Gibco), penicillin and streptomycin (Gibco) at a final concentration of 100 U/ml and 100 µg/ml and L-Glutamine (Gibco) at a final concentration of 2 mM. After filtering by a 40 µm strainer, cells were washed once with phosphate-buffered saline (PBS, Gibco and put into RPMI medium (Gibco) medium supplemented with 20 % FBS (Gibco) and 10 % dimethyl sulfoxide (DMSO, Serva), and then cryopreserved in liquid nitrogen until further analysis. an

*Quantification of immunohistochemical staining*

Formalin fixed lymph node tissue were processed through the hospital's routine immunohistochemistry pipeline and thereby stained for CD3, PAX5 and Ki67 (all Ventana). After completion of diagnostics, the corresponding slides were scanned for a subset of patients (n = 7). To quantify the frequencies of B and T cells, the open source software QuPath (v0.1.2) was used for PAX5 or CD3 stained slides according to the recommended workflow [57]. After detection of about 100.000 cells per slide, the measurements were exported and further analyzed using R. We visualized the intracellular signal of diaminobenzidine staining of all detected events in a histogram. For the staining of PAX5 and CD3 we observed two clear peaks for all samples and set a threshold in between. Cells with an intracellular signal of CD3 or PAX5 greater than this threshold were regarded as T cells or B cells, respectively. The proportion of $Ki67^+$ cells was obtained from routine pathology reports.

*Surface and intracellular staining by flow cytometry*

As described above, lymph node derived cells were thawed and stained for viability using a fixable viability dye e506 (Thermo Fisher Scientific) and for different surface markers depending on the experimental setup. The following surface antibodies were used: anti-CD3-PerCP/Cy5.5, anti-CD3-APC, anti-CD19-BV421, anti-kappa-PE, anti-kappa-FITC, anti-lambda-PE/Dazzle, anti-CD22-APC, anti-CD24-BV785, anti-CD27-PE-Cy7, anti-CD32-PE, anti-CD44-PE, anti-CD48-PE, anti-CD62L-PE/Cy7, anti-CD10-APC-Cy7, anti-CD4-AF700, anti-CD8-FITC, anti-PD1-BV421 and anti-ICOS-PE/Dazzle (all Biolegend). In case of

519 subsequent intracellular staining, cells were fixed and permeabilized with the intracellular
520 fixation/permeabilization buffer set (Thermo Fisher Scientific) and stained with anti-MYC-
521 AF647 (Thermo Fisher Scientific), anti-FoxP3-AF647 (BD Biosciences), or adequate isotype
522 controls (Thermo Fisher Scientific, BD Biosciences). Cells were then analyzed with an LSR
523 Fortessa (BD Biosciences) and FACSDiva (BD Biosciences, Version 8)
524

525 *Estimating the proportion of malignant and non-malignant B cells by flow cytometry*

526 Staining for expression of the light chains (kappa, lambda) is a well-established tool to identify
527 the accumulation of light chain restricted, malignant B cells [58]. Lymph node derived cells
528 were stained as described above. In case of a kappa$^+$ or lambda$^+$ B cell population greater than
529 80 %, we regarded this population as light chain restricted and therefore as malignant. We
530 further assumed that the ratio of kappa$^+$ versus lambda$^+$ B cells among the potentially remaining
531 non-malignant B cells is still balanced. Therefore, there must be roughly the same proportion
532 of non-malignant B cells among those carrying the restricted type of light chain. This ends up
533 in the following formula to estimate the proportion of malignant cells:

534 $$\text{Proportion}_{\text{Bcells\_malignant}} \approx \text{Proportion}_{\text{Bcells\_restricted}} - \text{Proportion}_{\text{Bcells\_not.restricted}}$$

535 In addition, cells without detectable expression of kappa or lambda light chain on protein level
536 were regarded as malignant cells because a loss of light chain expression is not observed in
537 non-malignant lymph nodes [59].
538

539 *Single cell sample preparation and RNA sequencing*

540 After thawing, cells were washed to remove DMSO as quickly as possible. We used the dead
541 cell removal kit (Miltenyi Biotec) for all samples to achieve a viability of at least 90%. The
542 preparation of the single cell suspensions, synthesis of cDNA and single cell libraries were
543 performed using the Chromium single cell v2 3' kit (10x Genomics) according to the
544 manufacturer's instructions. Each was sequenced on one NextSeq 550 lane (Illumina).
545

546 *Subclone specific drug screening*

547 58 different drugs at 5 different concentrations (Supplementary Table 5) and a suitable number
548 of DMSO controls were prepared in 384 well plates. DMSO concentration was kept equally at
549 0.2 % in all wells. Lymph node cells were thawed in a 37°C water bath and DMSO containing
550 freezing medium was removed as quickly as possible to reduce cytotoxic effects. Afterwards,
551 lymph node cells were rolled for 3 hours in RPMI medium supplemented with penicillin and

streptomycin (Gibco) at a final concentration of 100 U/ml and 100 µg/ml, L-glutamine (Gibco) at a final concentration of 2 mM and with 10 % human AB male serum (Sigma). Cells were seeded at a cell count of 50,000 in 50 µl per well. After 48 hours, cells were washed once with staining buffer [PBS (Gibco) supplemented with 1% FBS and 0.5 % ethylenediaminetetraacetic acid (EDTA, Sigma Aldrich)]. Cells were subsequently stained with fixable viability dye e506 (Thermo Fisher Scientific), anti-CD3-APC, anti-CD19-BV421 and anti-CD48-PE, anti-CD62L-PE/Cy7 or anti-kappa-FITC, anti-lambda-PE/Dazzle, anti-CD10-APC/Cy7, anti-CD27-PE/Cy7, anti-CD32-PE (all Biolegend). After staining the microtiter plate was washed twice with staining buffer. Then, cells were fixed using paraformaldehyde at a final concentration of 2 % for 15 min at room temperature and washed with staining buffer. Fixed cells were analyzed with an LSR II and FACSDiva (BD Biosciences, Version 8) equipped with a high throughput sampler (HTS) system (BD Biosciences). Approximately 5,000 to 10,000 events were recorded per well. Flow cytometry data was analyzed using FlowJo software (Tree Star). The gating strategy is illustrated in Supplementary Figure 8. We ruled out that significant up- or downregulation of subclone-discriminating surface antigens confound subclone-specific drug response assessment by evaluating the fluorescence intensity of corresponding markers before and after drug treatment (Supplementary Figure 10).

*Fluorescence-activated cell sorting of B cell subclones*

Lymph node cells were stained as described above. Sorting was performed at a FACS Aria Fusion (BD Biosciences). We sorted either for e506$^-$ CD3$^-$ CD19$^+$ CD48$^-$ CD62L$^-$ and e506$^-$ CD3$^-$ CD19$^+$ CD48$^-$ CD62L$^-$ (DLBCL1) or for e506$^-$ CD3$^-$ CD19$^+$CD10$^-$, e506$^-$ CD3$^-$ CD19$^+$ CD10$^+$ kappa$^+$, CD32$^{low}$ and e506$^-$ CD3$^-$ CD19$^+$ CD10$^+$ kappa$^+$, CD32$^{high}$ cells (tFL). The gating strategy is illustrated in Supplementary Figure 8. All relevant fractions were analyzed post-sorting to confirm a purity of at least 95 %.

*Whole genome and whole exome sequencing*

DNA was extracted using the DNeasy mini kit (Qiagen) according to the manufacturers protocol, followed by quality control using gel electrophoresis and a TapeStation 2200 system (Agilent). Samples were prepared either for WGS or WES, as previously described [60]. Exome capturing was performed using SureSelect Human All Exon V5 in-solution capture reagents (Agilent). If samples were destined for WES on an Illumina HiSeq 2500 instrument, then 1.5 µg genomic DNA were fragmented to 150 to 200 bp insert size with a Covaris S2 device, and 250 ng of Illumina adapter-containing libraries were hybridized with exome baits at 65°C for

16 hours. If samples were destined for WES on an Illumina HiSeq 4000 instrument, then 200 ng genomic DNA were fragmented to 300 bp insert size with a Covaris LE220 or E220 device, and 750 ng of adapter-containing libraries were hybridized with exome baits at 65°C for 16 hours. If samples were destined for WGS on an Illumina HiSeq X instrument, then 100 ng of genomic DNA were fragmented to 450 bp insert size with a Covaris LE220 or E220 device, and libraries were prepared using the TruSeq Nano Kit (Illumina). On all platforms paired-end sequencing was carried out according to the manufacturer's recommendations, yielding read lengths of 101 bp (4000) or 151 bp (HiSeq X).

*Single cell RNA sequencing data processing*

The Cell Ranger analysis pipeline (v2.1, 10x Genomics) was used to demultiplex the raw base call files and to convert them into FASTQ files. FASTQ files were aligned to the reference genome (hg38) and filtered. Final numbers of cell barcodes, unique molecular identifiers (UMI) per cell, median genes and sequencing saturation are summarized in Supplementary Table 8.

*Filtering and normalizing single cell RNA sequencing data*

The R package Seurat [61] (v2.3.3) was used to perform quality control and normalization. Gene count per cell, UMI count per cell and the percentage of mitochondrial and ribosomal transcripts were computed using the functions of the Seurat package. Genes expressed in three cells or fewer were excluded from downstream analysis. Libraries with a percentage of mitochondrial transcripts greater than 5%, along with those with less than 200 genes were filtered out prior to further analysis. Since aggressive lymphomas displayed higher gene and UMI count, the upper limit was set with regard to each sample. Counts were adjusted for cell-specific sampling ("normalized") using the LogNormalize function with the default scale factor of 10,000.

*Assessing the cell cycle state using scRNA-seq data*

The cell cycle state was assessed using the gene set and scoring system, described by Tirosh and colleagues [8]. Briefly, the S-Score and the $G_2$M-Score were calculated based on a list of 43 S phase-specific and 54 $G_2$ or M phase-specific genes. The calculation of the actual scores was performed using the CellCycleScoring function of the Seurat R package.

*Analysis of ligand-receptor interactions in scRNA-Seq data*

We used the CellPhoneDB database [37] as basis for potential cell-cell interactions, but expanded the list by important B to T cell interactions (Supplementary Table 4). To assess the significance of each interaction, we adapted a statistical framework recently described by Vento-Tormo and colleagues [37] to our purpose. Importantly, we considered only genes which were expressed in 5 % of at least one cell type.

Briefly, we performed pairwise comparisons between the different T and B cell subtypes for each ligand-receptor pair and sample. For each combination of two different cell types and each ligand-receptor-pair, we permuted the cluster labels of cells at least 1,000 times and determined the mean interaction score (mean expression of ligand in cell type A times mean expression of receptor in cell type B). A p value was determined by calculating the proportion of permuted interaction scores which were by hazard higher than the actual interaction score. All interactions were calculated sample-wise. To determine which interactions were most relevant across different samples, we calculated the mean interaction scores and combined the different p values using the Fisher's method. Then, p values were corrected using the Benjamini-Hochberg method. The R code is available on our GitHub repository (see code availability statement below).

*Combining data from different samples and batch correction*

After identification of the different cell types the data sets were split into non-B cells or B cells using the SubsetData function. Then the respective subsets were combined using the MergeSeurat function. Putative batch effects between two runs, were corrected by the mutual nearest neighbors (MNN) technique [62] which is implemented in the scran Bioconductor package (v1.10.2).

*Clustering and dimensionality reduction techniques*

SNN (Shared-nearest neighbor)-based clustering, t-SNE and UMAP visualization were performed using the FindClusters, RunTSNE and RunUMAP functions within the Seurat package [61]. Each of these were performed on the basis of a principal component analysis which was performed using the RunPCA function of the Seurat package. The same parameters were applied to all samples. UMAP was used instead of t-SNE for combined data sets because it is significantly faster than t-SNE and better preserves aspects of global structure in larger data sets [28]. Differentially expressed genes between the clusters were identified using the FindMarkers or FindAllMarkers functions within the Seurat package [61]. Differentially

652 expressed genes between malignant B cell clusters can be browsed interactively using an html
653 file (see data sharing statement below).
654
655 *Gene set enrichment analysis*
656 Gene set enrichment analysis (GSEA) was performed using the GSEA java desktop application
657 [63, 64] and the Molecular Signatures Database (MSigDB, v6.2) provided by the Broad Institute
658 [63, 65]. Differentially expressed genes of two groups were used to determine significantly-
659 enriched gene sets.
660
661 *WES and WGS data processing*
662 Alignment of sequencing read pairs and variant calling were performed as recently described
663 [66]. Briefly, reads were mapped to human reference genome (hg19) with bwa-mem (version
664 0.7.8, minimum base quality threshold set to zero [-T 0], remaining settings left to default) [67].
665 Subsequently, reads were coordinate-sorted with bamsort (compression option set to fast) and
666 duplicate read pairs were marked with bammarkduplicates (compression option set to best)
667 (both part of biobambam package version 0.0.148).
668 SNV and indels in matched tumor normal pairs were identified using the internal DKFZ variant
669 calling workflows based on samtools/bcftools 0.1.19 with additional custom filters (optimized
670 for somatic variant calling by deactivating the pval-threshold in bcftools) and Platypus 0.8.1,
671 respectively, as described previously [66]. Gene annotation of variants was done with
672 Annovar [68]. The variants were annotated with dbSNP141, 1000 Genomes (phase 1), Gencode
673 mapability track, UCSC High Seq Depth track, UCSC Simple-Tandem repeats, UCSC Repeat-
674 Masker, DUKE-Excluded, DAC-Blacklist, UCSC Selfchain. These annotation tracks were used
675 to determine a confidence score for each variant by a heuristic punishment scheme and only
676 high confidence variants were kept for further analysis. In addition, variants with strong read
677 biases according to the strand bias filter were removed.
678 Genomic structural rearrangements (SVs) were identified using the SOPHIA algorithm
679 (unpublished, source code available at https://bitbucket.org/utoprak/sophia/). Briefly,
680 supplementary alignments as produced by bwa-mem are used as indicators of potential
681 underlying SVs. Candidates are filtered by comparing them to a background control set of
682 sequencing data obtained using normal blood samples from a background population database
683 of 3261 patients from published TCGA and ICGC studies as well as published and unpublished
684 studies of the German Cancer Research Center (DKFZ).

Allele-specific CNV were detected using ACEseq (allele-specific copy number estimation from WGS) [69] for WGS data and CNVkit for WES data [70]. ACEseq determines absolute allele-specific copy numbers as well as tumor ploidy and tumor cell content based on coverage ratios of tumor and control as well as the B-allele frequency (BAF) of heterozygous single-nucleotide polymorphisms (SNPs). SVs called by SOPHIA were incorporated to improve genome segmentation.

*Multi tumor comparison*

To compare multi tumor samples of the same donor, every SNV position in each sample was determined using samtools mpileup 1.6. At each of these SNV positions, the variant allele fraction was determined by calculating the ratio between the number of variant reads and the total coverage at that position. To correct the variant allele fraction for actual tumor cell content, a scaling factor was incorporated, comprising ploidy and total copy number (TCN) estimates obtained from ACEseq/CNVkit. Specifically, the scaling factor is obtained as the ratio between purity corrected number of alleles in the tumor (TCN_tumor purity_tumor) and purity corrected total number of alleles in the sample ((TCN_tumor * purity_tumor) + 2 * (1 - purity_tumor)).

*Aberrant cell fraction estimation from LOH*

To determine aberrant cell fractions, the minor allele-frequency (MAF, ratio between number of reads of minor allele and total coverage at given position) of single nucleotide polymorphism (SNP) was estimated for selected regions harboring a loss of heterozygosity (LOH) or a copy number neutral LOH (CN-LOH) in the tumor sample. Information on SNP location was received from matched-control SNV calling. To select heterozygous SNP, only SNP with a MAF $\geq 0.3$ in the control were retained. Subsequently, MAF values of the selected SNP were calculated for the tumor samples. For exome samples, only SNP within the targeted capture regions were kept. The mean of the respective tumor MAF values was calculated and the aberrant cell fraction (ACF) was estimated as follows:

$$ACF_{LOH} = 1 - 2 \cdot mean\,(MAF)\,;\; ACF_{CN-LOH} = \frac{1 - 2 \cdot mean\,(MAF)}{1 - mean\,(MAF)}$$

*Data sharing statement*

The single cell expression data of merged B and T cell UMAP plots (Figure 2A/B and Figure 3A/B) are available for easy-to-use interactive browsing: https://www.zmbh.uni-heidelberg.de/Anders/scLN-index.html.

718 The raw single cell count tables can be downloaded here doi.org/10.11588/data/VRJUNV. This
719 link will be activated upon publication and is accessible without further restriction.
720 Differentially expressed genes between B cell clusters can be browsed in an interactive html
721 file (Supplementary File 1).
722
723 *Code availability statement*
724 R codes used for data analysis are available at our GitHub repository without further restriction
725 (www.github.com/DietrichLab/scLymphomaExplorer).

## References


1. Burrell RA, McGranahan N, Bartek J, Swanton C. The causes and consequences of genetic heterogeneity in cancer evolution. *Nature* 2013 09/18/online; **501:** 338.

2. Swanton C. Intratumor heterogeneity: evolution through space and time. *Cancer research* 2012; **72**(19)**:** 4875-4882.

3. McGranahan N, Swanton C. Clonal Heterogeneity and Tumor Evolution: Past, Present, and the Future. *Cell* 2017 Feb 9; **168**(4)**:** 613-628.

4. Kim IS, Zhang XH. One microenvironment does not fit all: heterogeneity beyond cancer cells. *Cancer Metastasis Rev* 2016 Dec; **35**(4)**:** 601-629.

5. Fridman WH, Pages F, Sautes-Fridman C, Galon J. The immune contexture in human tumours: impact on clinical outcome. *Nat Rev Cancer* 2012 Mar 15; **12**(4)**:** 298-306.

6. Navin N, Kendall J, Troge J, Andrews P, Rodgers L, McIndoo J*, et al.* Tumour evolution inferred by single-cell sequencing. *Nature* 2011 Apr 7; **472**(7341)**:** 90-94.

7. Wang Y, Navin NE. Advances and applications of single-cell sequencing technologies. *Mol Cell* 2015 May 21; **58**(4)**:** 598-609.

8. Tirosh I, Izar B, Prakadan SM, Wadsworth MH, 2nd, Treacy D, Trombetta JJ*, et al.* Dissecting the multicellular ecosystem of metastatic melanoma by single-cell RNA-seq. *Science* 2016 Apr 8; **352**(6282)**:** 189-196.

9. Gao R, Kim C, Sei E, Foukakis T, Crosetto N, Chan LK*, et al.* Nanogrid single-nucleus RNA sequencing reveals phenotypic diversity in breast cancer. *Nat Commun* 2017 Aug 9; **8**(1)**:** 228.

10. Yuan J, Sims PA. An Automated Microwell Platform for Large-Scale Single Cell RNA-Seq. *Sci Rep* 2016 Sep 27; **6:** 33883.

11. Islam S, Zeisel A, Joost S, La Manno G, Zajac P, Kasper M*, et al.* Quantitative single-cell RNA-seq with unique molecular identifiers. *Nat Methods* 2014 Feb; **11**(2)**:** 163-166.

12. Patel AP, Tirosh I, Trombetta JJ, Shalek AK, Gillespie SM, Wakimoto H*, et al.* Single-cell RNA-seq highlights intratumoral heterogeneity in primary glioblastoma. *Science* 2014 Jun 20; **344**(6190)**:** 1396-1401.

13. Ramskold D, Luo S, Wang YC, Li R, Deng Q, Faridani OR*, et al.* Full-length mRNA-Seq from single-cell levels of RNA and individual circulating tumor cells. *Nat Biotechnol* 2012 Aug; **30**(8)**:** 777-782.

14. Powell AA, Talasaz AH, Zhang H, Coram MA, Reddy A, Deng G*, et al.* Single cell profiling of circulating tumor cells: transcriptional heterogeneity and diversity from breast cancer cell lines. *PLoS One* 2012; **7**(5)**:** e33788.

15. Kim C, Gao R, Sei E, Brandt R, Hartman J, Hatschek T, *et al.* Chemoresistance Evolution in Triple-Negative Breast Cancer Delineated by Single-Cell Sequencing. *Cell* 2018 May 3; **173**(4)**:** 879-893 e813.

16. Teras LR, DeSantis CE, Cerhan JR, Morton LM, Jemal A, Flowers CR. 2016 US lymphoid malignancy statistics by World Health Organization subtypes. *CA Cancer J Clin* 2016 Sep 12.

17. Wagner-Johnston ND, Link BK, Byrtek M, Dawson KL, Hainsworth J, Flowers CR, *et al.* Outcomes of transformed follicular lymphoma in the modern era: a report from the National LymphoCare Study (NLCS). *Blood* 2015 Aug 13; **126**(7)**:** 851-857.

18. Crump M, Neelapu SS, Farooq U, Van Den Neste E, Kuruvilla J, Westin J, *et al.* Outcomes in refractory diffuse large B-cell lymphoma: results from the international SCHOLAR-1 study. *Blood* 2017 Oct 19; **130**(16)**:** 1800-1808.

19. Philip T, Armitage JO, Spitzer G, Chauvin F, Jagannath S, Cahn JY, *et al.* High-dose therapy and autologous bone marrow transplantation after failure of conventional chemotherapy in adults with intermediate-grade or high-grade non-Hodgkin's lymphoma. *N Engl J Med* 1987 Jun 11; **316**(24)**:** 1493-1498.

20. Bartlett NL, Costello BA, LaPlant BR, Ansell SM, Kuruvilla JG, Reeder CB, *et al.* Single-agent ibrutinib in relapsed or refractory follicular lymphoma: a phase 2 consortium trial. *Blood* 2018 Jan 11; **131**(2)**:** 182-190.

21. Winter AM, Landsburg DJ, Mato AR, Isaac K, Hernandez-Ilizaliturri FJ, Reddy N, *et al.* A multi-institutional outcomes analysis of patients with relapsed or refractory DLBCL treated with ibrutinib. *Blood* 2017 Aug 9.

22. Horna P, Olteanu H, Kroft SH, Harrington AM. Flow cytometric analysis of surface light chain expression patterns in B-cell lymphomas using monoclonal and polyclonal antibodies. *Am J Clin Pathol* 2011 Dec; **136**(6)**:** 954-959.

23. Schreiber RD, Old LJ, Smyth MJ. Cancer immunoediting: integrating immunity's roles in cancer suppression and promotion. *Science* 2011 Mar 25; **331**(6024)**:** 1565-1570.

24. Challa-Malladi M, Lieu YK, Califano O, Holmes AB, Bhagat G, Murty VV, *et al.* Combined genetic inactivation of beta2-Microglobulin and CD58 reveals frequent escape from immune recognition in diffuse large B cell lymphoma. *Cancer Cell* 2011 Dec 13; **20**(6)**:** 728-740.

25. Xu-Monette ZY, Zhou J, Young KH. PD-1 expression and clinical PD-1 blockade in B-cell lymphomas. *Blood* 2018 Jan 4; **131**(1)**:** 68-83.

26. Sun LL, Ellerman D, Mathieu M, Hristopoulos M, Chen X, Li Y, *et al.* Anti-CD20/CD3 T cell-dependent bispecific antibody for the treatment of B cell malignancies. *Sci Transl Med* 2015 May 13; **7**(287)**:** 287ra270.

27. Os A, Burgler S, Ribes AP, Funderud A, Wang D, Thompson KM, *et al.* Chronic lymphocytic leukemia cells are activated and proliferate in response to specific T helper cells. *Cell Rep* 2013 Aug 15; **4**(3)**:** 566-577.

28. Becht E, McInnes L, Healy J, Dutertre CA, Kwok IWH, Ng LG*, et al.* Dimensionality reduction for visualizing single-cell data using UMAP. *Nat Biotechnol* 2018 Dec 3.

29. Schaerli P, Willimann K, Lang AB, Lipp M, Loetscher P, Moser B. CXC chemokine receptor 5 expression defines follicular homing T cells with B cell helper function. *J Exp Med* 2000 Dec 4; **192**(11)**:** 1553-1562.

30. Breitfeld D, Ohl L, Kremmer E, Ellwart J, Sallusto F, Lipp M*, et al.* Follicular B helper T cells express CXC chemokine receptor 5, localize to B cell follicles, and support immunoglobulin production. *J Exp Med* 2000 Dec 4; **192**(11)**:** 1545-1552.

31. Dorfman DM, Shahsafaei A. CD200 (OX-2 membrane glycoprotein) is expressed by follicular T helper cells and in angioimmunoblastic T-cell lymphoma. *Am J Surg Pathol* 2011 Jan; **35**(1)**:** 76-83.

32. Weber JP, Fuhrmann F, Feist RK, Lahmann A, Al Baz MS, Gentz LJ*, et al.* ICOS maintains the T follicular helper cell phenotype by down-regulating Kruppel-like factor 2. *J Exp Med* 2015 Feb 9; **212**(2)**:** 217-233.

33. Yang ZZ, Grote DM, Ziesmer SC, Xiu B, Novak AJ, Ansell SM. PD-1 expression defines two distinct T-cell sub-populations in follicular lymphoma that differentially impact patient survival. *Blood Cancer J* 2015 Feb 20; **5:** e281.

34. Yamazaki T, Nagumo H, Hayashi T, Sugane K, Agematsu K. CD72-mediated suppression of human naive B cell differentiation by down-regulating X-box binding protein 1. *Eur J Immunol* 2005 Aug; **35**(8)**:** 2325-2334.

35. Klein U, Rajewsky K, Kuppers R. Human immunoglobulin (Ig)M+IgD+ peripheral blood B cells expressing the CD27 cell surface antigen carry somatically mutated variable region genes: CD27 as a general marker for somatically mutated (memory) B cells. *J Exp Med* 1998 Nov 2; **188**(9)**:** 1679-1689.

36. Hans CP, Weisenburger DD, Greiner TC, Gascoyne RD, Delabie J, Ott G*, et al.* Confirmation of the molecular classification of diffuse large B-cell lymphoma by immunohistochemistry using a tissue microarray. *Blood* 2004 Jan 1; **103**(1)**:** 275-282.

37. Vento-Tormo R, Efremova M, Botting RA, Turco MY, Vento-Tormo M, Meyer KB*, et al.* Single-cell reconstruction of the early maternal-fetal interface in humans. *Nature* 2018 Nov; **563**(7731)**:** 347-353.

38. Shirota H, Klinman DM, Ito SE, Ito H, Kubo M, Ishioka C. IL4 from T Follicular Helper Cells Downregulates Antitumor Immunity. *Cancer Immunol Res* 2017 Jan; **5**(1)**:** 61-71.

39. Aguilar-Hernandez MM, Blunt MD, Dobson R, Yeomans A, Thirdborough S, Larrayoz M*, et al.* IL-4 enhances expression and function of surface IgM in CLL cells. *Blood* 2016 Jun 16; **127**(24)**:** 3015-3025.

40. Peter-Martin B, Giles H, Kolb C, Rabe S, Roider T, Knoll M*, et al.* Systematic Investigation of Microenvironmental Drug Resistance Mechanisms in Chronic Lymphocytic Leukemia. *ASH Abstract Book* 2019.

41. Spolski R, Leonard WJ. IL-21 and T follicular helper cells. *Int Immunol* 2010 Jan; **22**(1)**:** 7-12.

42. Gu-Trantien C, Migliori E, Buisseret L, de Wind A, Brohee S, Garaud S*, et al.* CXCL13-producing TFH cells link immune suppression and adaptive memory in human breast cancer. *JCI Insight* 2017 Jun 2; **2**(11).

43. DiToro D, Winstead CJ, Pham D, Witte S, Andargachew R, Singer JR*, et al.* Differential IL-2 expression defines developmental fates of follicular versus nonfollicular helper T cells. *Science* 2018 Sep 14; **361**(6407).

44. Chapuy B, Stewart C, Dunford AJ, Kim J, Kamburov A, Redd RA*, et al.* Molecular subtypes of diffuse large B cell lymphoma are associated with distinct pathogenic mechanisms and outcomes. *Nat Med* 2018 May; **24**(5)**:** 679-690.

45. Andor N, Simonds EF, Czerwinski DK, Chen J, Grimes SM, Wood-Bouwens C*, et al.* Single-cell RNA-Seq of follicular lymphoma reveals malignant B-cell types and coexpression of T-cell immune checkpoints. *Blood* 2019 Mar 7; **133**(10)**:** 1119-1129.

46. Liberzon A, Birger C, Thorvaldsdottir H, Ghandi M, Mesirov JP, Tamayo P. The Molecular Signatures Database (MSigDB) hallmark gene set collection. *Cell Syst* 2015 Dec 23; **1**(6)**:** 417-425.

47. Dietrich S, Oles M, Lu J, Sellner L, Anders S, Velten B*, et al.* Drug-perturbation-based stratification of blood cancer. *J Clin Invest* 2018 Jan 2; **128**(1)**:** 427-445.

48. Delmore JE, Issa GC, Lemieux ME, Rahl PB, Shi J, Jacobs HM*, et al.* BET bromodomain inhibition as a therapeutic strategy to target c-Myc. *Cell* 2011 Sep 16; **146**(6)**:** 904-917.

49. Chapuy B, McKeown MR, Lin CY, Monti S, Roemer MG, Qi J*, et al.* Discovery and characterization of super-enhancer-associated dependencies in diffuse large B cell lymphoma. *Cancer Cell* 2013 Dec 9; **24**(6)**:** 777-790.

50. Navin NE. The first five years of single-cell cancer genomics and beyond. *Genome Res* 2015; **25**(10)**:** 1499-1507.

51. Ledergor G, Weiner A, Zada M, Wang S-Y, Cohen YC, Gatt ME*, et al.* Single cell dissection of plasma cell heterogeneity in symptomatic and asymptomatic myeloma. *Nature Medicine* 2018 2018/12/01; **24**(12)**:** 1867-1876.

52. Puram SV, Tirosh I, Parikh AS, Patel AP, Yizhak K, Gillespie S*, et al.* Single-Cell Transcriptomic Analysis of Primary and Metastatic Tumor Ecosystems in Head and Neck Cancer. *Cell* 2017 Dec 14; **171**(7)**:** 1611-1624 e1624.

53. de Boer B, Prick J, Pruis MG, Keane P, Imperato MR, Jaques J*, et al.* Prospective Isolation and Characterization of Genetically and Functionally Distinct AML Subclones. *Cancer Cell* 2018 Oct 8; **34**(4)**:** 674-689 e678.

54. Milpied P, Cervera-Marzal I, Mollichella M-L, Tesson B, Brisou G, Traverse-Glehen A*, et al.* Human germinal center transcriptional programs are de-synchronized in B cell lymphoma. *Nature Immunology* 2018 2018/09/01; **19**(9)**:** 1013-1024.

55. Byford ET, Carr M, Ladikou E, Ahearne MJ, Wagner SD. Circulating Tfh1 (cTfh1) cell numbers and PD1 expression are elevated in low-grade B-cell non-Hodgkin's lymphoma and cTfh gene expression is perturbed in marginal zone lymphoma. *PLoS One* 2018; **13**(1)**:** e0190468.

56. Li J, Byrne KT, Yan F, Yamazoe T, Chen Z, Baslan T*, et al.* Tumor Cell-Intrinsic Factors Underlie Heterogeneity of Immune Cell Infiltration and Response to Immunotherapy. *Immunity* 2018 Jul 17; **49**(1)**:** 178-193 e177.

57. Bankhead P, Loughrey MB, Fernández JA, Dombrowski Y, McArt DG, Dunne PD*, et al.* QuPath: Open source software for digital pathology image analysis. *Scientific Reports* 2017 2017/12/04; **7**(1)**:** 16878.

58. Ratech H, Litwin S. Surface immunoglobulin light chain restriction in B-cell non-Hodgkin's malignant lymphomas. *Am J Clin Pathol* 1989 May; **91**(5)**:** 583-586.

59. Kaleem Z, Zehnbauer BA, White G, Zutter MM. Lack of expression of surface immunoglobulin light chains in B-cell non-Hodgkin lymphomas. *Am J Clin Pathol* 2000 Mar; **113**(3)**:** 399-405.

60. Heining C, Horak P, Uhrig S, Codo PL, Klink B, Hutter B*, et al.* NRG1 Fusions in KRAS Wild-Type Pancreatic Cancer. *Cancer Discov* 2018 Sep; **8**(9)**:** 1087-1095.

61. Butler A, Hoffman P, Smibert P, Papalexi E, Satija R. Integrating single-cell transcriptomic data across different conditions, technologies, and species. *Nat Biotechnol* 2018 Jun; **36**(5)**:** 411-420.

62. Haghverdi L, Lun ATL, Morgan MD, Marioni JC. Batch effects in single-cell RNA-sequencing data are corrected by matching mutual nearest neighbors. *Nature Biotechnology* 2018 04/02/online; **36:** 421.

63. Subramanian A, Tamayo P, Mootha VK, Mukherjee S, Ebert BL, Gillette MA*, et al.* Gene set enrichment analysis: a knowledge-based approach for interpreting genome-wide expression profiles. *Proc Natl Acad Sci U S A* 2005 Oct 25; **102**(43)**:** 15545-15550.

64. Mootha VK, Lindgren CM, Eriksson KF, Subramanian A, Sihag S, Lehar J*, et al.* PGC-1alpha-responsive genes involved in oxidative phosphorylation are coordinately downregulated in human diabetes. *Nat Genet* 2003 Jul; **34**(3)**:** 267-273.

65. Liberzon A, Subramanian A, Pinchback R, Thorvaldsdottir H, Tamayo P, Mesirov JP. Molecular signatures database (MSigDB) 3.0. *Bioinformatics* 2011 Jun 15; **27**(12)**:** 1739-1740.

66. López C, Kleinheinz K, Aukema SM, Rohde M, Bernhart SH, Hübschmann D*, et al.* Genomic and transcriptomic changes complement each other in the pathogenesis of sporadic Burkitt lymphoma. *Nature Communications* 2019 2019/03/29; **10**(1)**:** 1459.

67. Li H, Handsaker B, Wysoker A, Fennell T, Ruan J, Homer N, *et al.* The Sequence Alignment/Map format and SAMtools. *Bioinformatics* 2009 Aug 15; **25**(16)**:** 2078-2079.

68. Wang K, Li M, Hakonarson H. ANNOVAR: functional annotation of genetic variants from high-throughput sequencing data. *Nucleic Acids Res* 2010 Sep; **38**(16)**:** e164.

69. Kleinheinz K, Bludau I, Hübschmann D, Heinold M, Kensche P, Gu Z, *et al.* ACEseq – allele specific copy number estimation from whole genome sequencing. *bioRxiv* 2017**:** 210807.

70. Talevich E, Shain AH, Botton T, Bastian BC. CNVkit: Genome-Wide Copy Number Detection and Visualization from Targeted DNA Sequencing. *PLoS Comput Biol* 2016 Apr; **12**(4)**:** e1004873.

# Figure 1

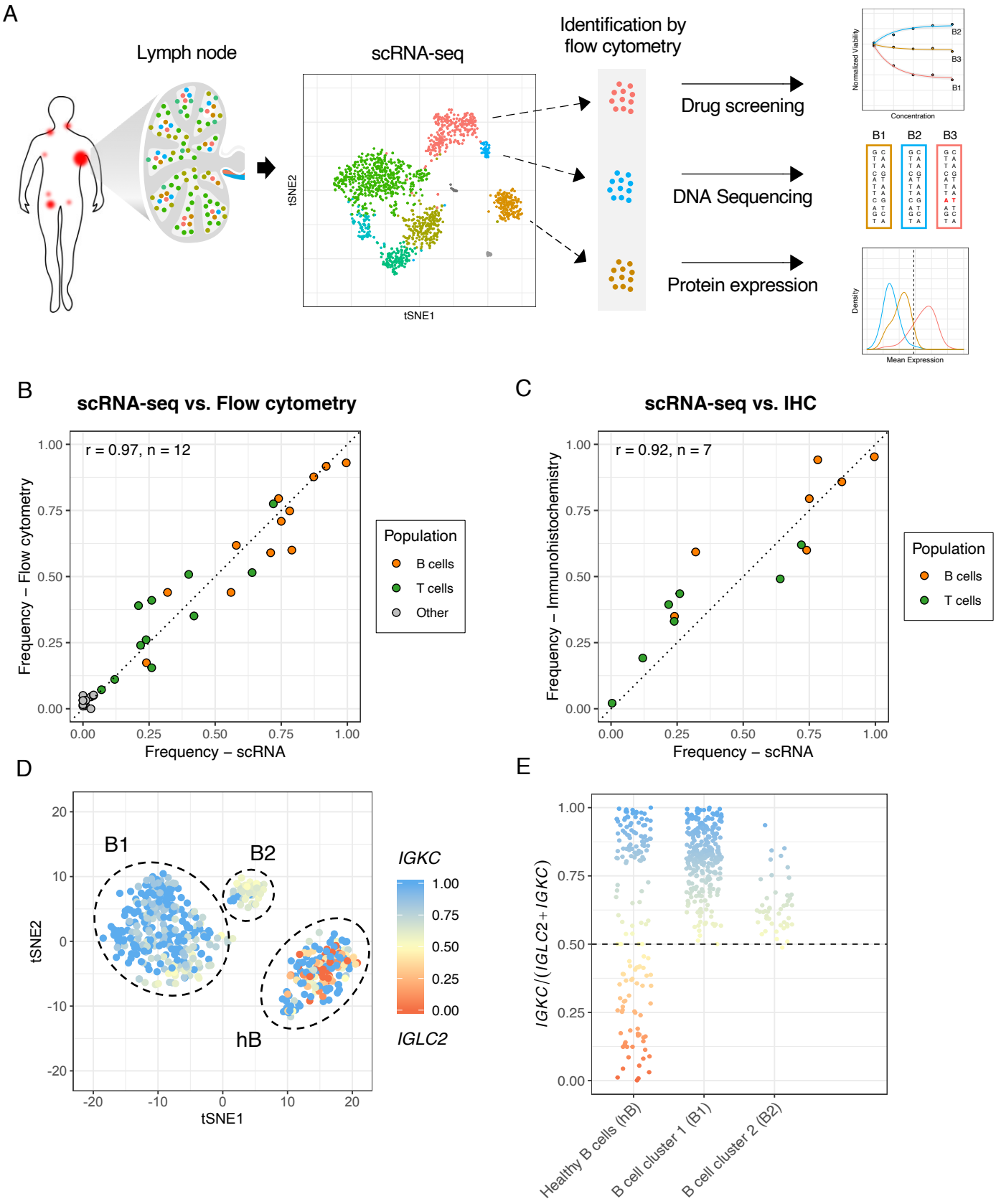
A
Lymph node
scRNA-seq
Identification by flow cytometry
tSNE2
tSNE1
Drug screening
DNA Sequencing
Protein expression
Normalized Viability
Concentration
B1
B2
B3
Density
Mean Expression
B
scRNA-seq vs. Flow cytometry
r = 0.97, n = 12
Frequency – Flow cytometry
Frequency – scRNA
Population
B cells
T cells
Other
C
scRNA-seq vs. IHC
r = 0.92, n = 7
Frequency – Immunohistochemistry
Frequency – scRNA
Population
B cells
T cells
D
B1
B2
hB
tSNE2
tSNE1
IGKC
IGLC2
E
IGKC/(IGLC2+IGKC)
Healthy B cells (hB)
B cell cluster 1 (B1)
B cell cluster 2 (B2)

**Figure 1. Identification of cell types using scRNA-seq.**

A) Schematic overview of the study design. B and C) Lymph node-derived B and T cells were quantified by scRNA-seq, flow cytometry and immunohistochemistry (IHC) of paraffin tissue sections (see Supplementary Figure 1 for details). The frequencies of B and T cells were correlated for B) scRNA-seq and flow cytometry or C) scRNA-seq and IHC. Pearson's correlation coefficients (r) and the number of samples included (n) are given in the left top corner. D and E) Illustration of the strategy to identify malignant B cells. Single cell RNA expression profiles of B cells derived from the tFL1 sample were visualized by t-SNE. The different B cell clusters are circled and labeled with hB (healthy B cells), B1 (B cell cluster 1) and B2 (B cell cluster 2). For each single B cell we calculated the the kappa light chain (IGKC) fraction *IGKC*/(*IGKC+IGLC2)* (see color code D and E). If this IGKC-fraction was > 0.5, we classified a B cell as a kappa positive and if this ratio was below 0.5 we classified the B cell as a lambda positive. The percentage of B cells either expressing kappa or lambda per transcriptionally distinct B cell cluster was calculated. The non-malignant healthy B cell (hB) cluster contained approximately 50% kappa and 50% lambda expressing B cells while the tow malignant cluster (B1, B2) contained B cells homogeneously expressing the kappa light chain.

# Figure 2

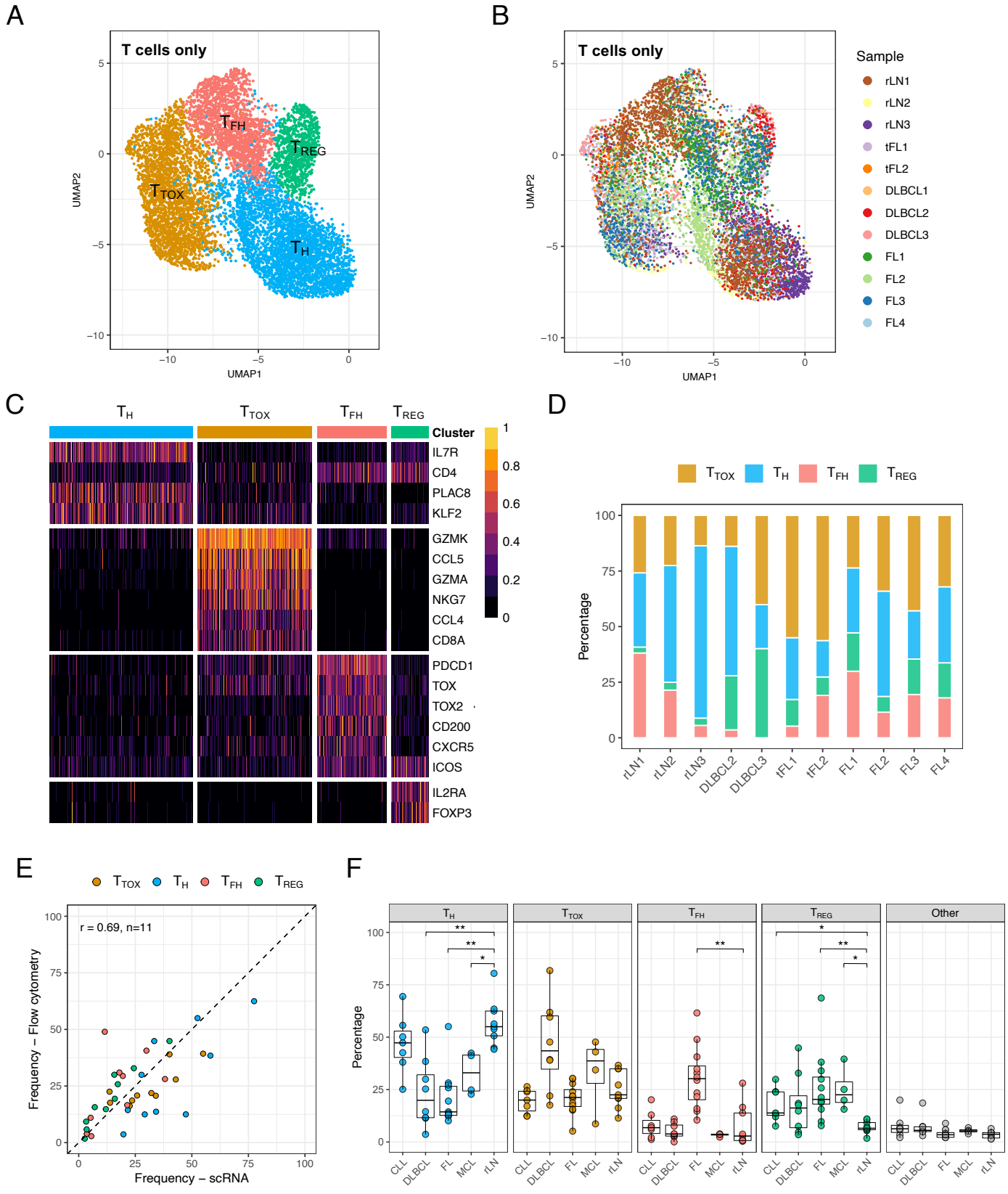


**Figure 2. The transcriptional heterogeneity of lymph node-derived T cells**

A and B) T cells from all samples were combined and jointly visualized using UMAP. Cells were colored with respect to their cluster of origin (A) or to their sample of origin (B). C) The heatmap shows differentially expressed genes, which were used to identify the T cell subsets: Cytotoxic T cells ($T_{TOX}$), conventional T helper cells ($T_H$), T follicular helper cells ($T_{FH}$), regulatory T cells ($T_{REG}$). Gene expression values were scaled to the

the maximum of each row. D) Stacked bar chart displaying the proportion of T cell subpopulations based on scRNA-seq identified in each sample. Note that the DLBCL1 sample is not shown here due to only five T cells identified in this sample. E and F) Single cell suspensions of lymph nodes derived from 39 different patients, including those passed to scRNA-seq, were characterized by flow cytometry. The four different T cell populations identified by single cell RNA-Seq were distinguished using the following marker panel: CD3, CD4, CD8, PD1, ICOS and FoxP3. Specifically, $T_H$ were identified based on $CD3^+CD4^+$ without the phenotype of $T_{FH}$ or $T_{REG}$; $T_{TOX}$ were identified based on $CD3^+CD8^+$; $T_{FH}$ were identified based on $CD3^+CD4^+$ $ICOS^{High}PD1^{High}$; and $T_{REG}$ were identified based on $CD3^+CD4^+FoxP3^+$. E) The frequencies based on flow cytometry were correlated with the frequencies based on scRNA-seq. Pearson's correlation coefficients (r) and the number of samples included (n) are given in the top left corner. Note that the DLBCL1 and tFL2 samples are not shown here due to the low number of T cells in the scRNA-seq data (DLBCL1) or the lack of material (tFL2). F) Frequencies for each subpopulation with regard to the sum of all T cells are shown. P values were calculated by the two-sided Wilcoxon's test comparing each Entity with rLN group, and corrected by Bonferroni method. Only significant differences are shown; ** ≙ p value ≤ 0.01, * ≙ p value ≤ 0.05. SNN: Shared-nearest-neighbor-based. UMAP: Uniform Manifold Approximation and Projection. rLN: Reactive lymph node. MCL: Mantle cell lymphoma. FL: Follicular lymphoma. DLBCL: Diffuse large B cell lymphoma, CLL: Chronic lymphocytic leukemia.

# Figure 3

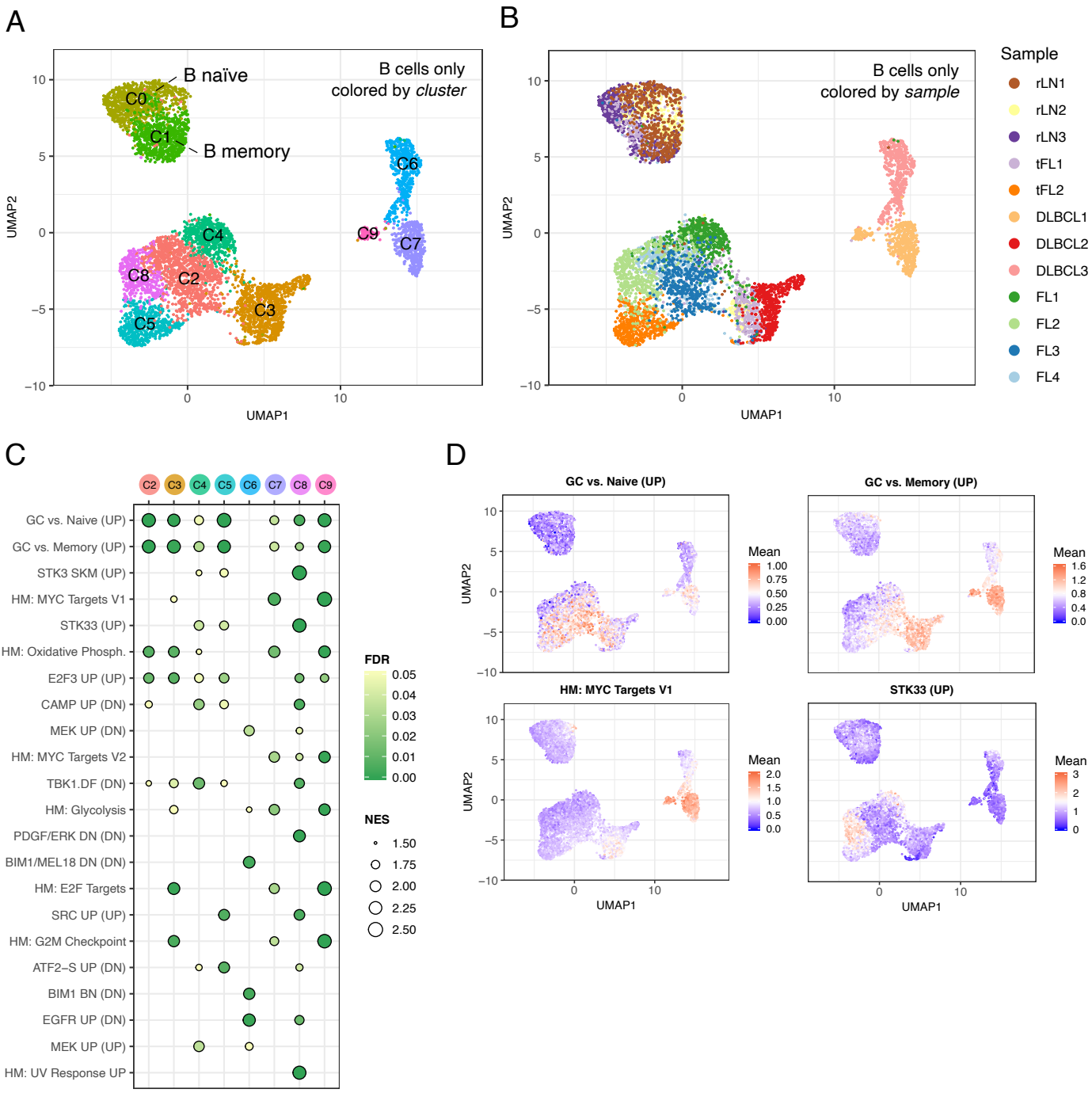


**Figure 3. Gene expression signatures driving B cell heterogeneity.**

A and B) Single cell RNA expression profiles from all B cells were combined and jointly visualized using UMAP. Cells are colored either by SNN-based clusters (A) or by sample (B). C) A gene set enrichment analysis was performed separately for each malignant cluster (C3 to C9) versus all healthy B cells (C0, C1). The four most enriched gene sets per sample are shown. Columns refer to cluster. Circles are coded by color (nominal FDR) and size (NES). Gene sets with NES > 1.5 are shown. D) Cells in UMAP plot were colored by the mean expression of enriched genes for four representative gene expression signatures. UMAP: Uniform Manifold Approximation and Projection. SNN: Shared-nearest-neighbor. FDR: False-positive detection rate. NES: Normalized enrichment score.

# Figure 4

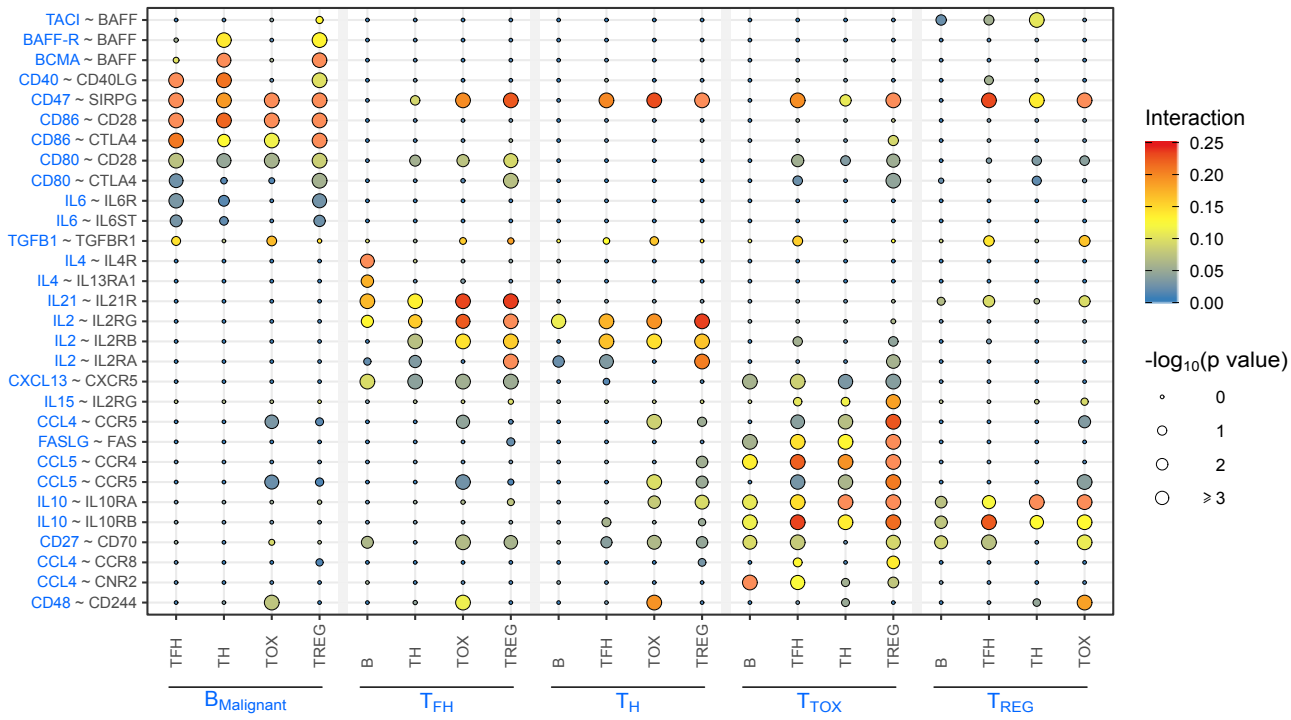


**Figure 4. Cellular crosstalk in B cell lymphoma within the lymph node microenvironment.**

Overview of most significant ligand-receptor interactions across all lymphoma samples, excluding DLBCL1 due to the low number of T cells. Circle size indicates negative $\log_{10}$ of adjusted p values which were determined by permutation test (see Methods for details). Color scheme visualizes interaction scores which were calculated by the mean expression of molecule 1 (blue) in cell type A (blue) and the mean expression of molecule 2 (black) in cell type B (black). Protein names instead of gene names were used for TACI (*TNFRSF13B*), BAFF-R (*TNFRSF13C*), BCMA (*TNFRSF17*) and BAFF (*TNFSF13B*).

# Figure 5

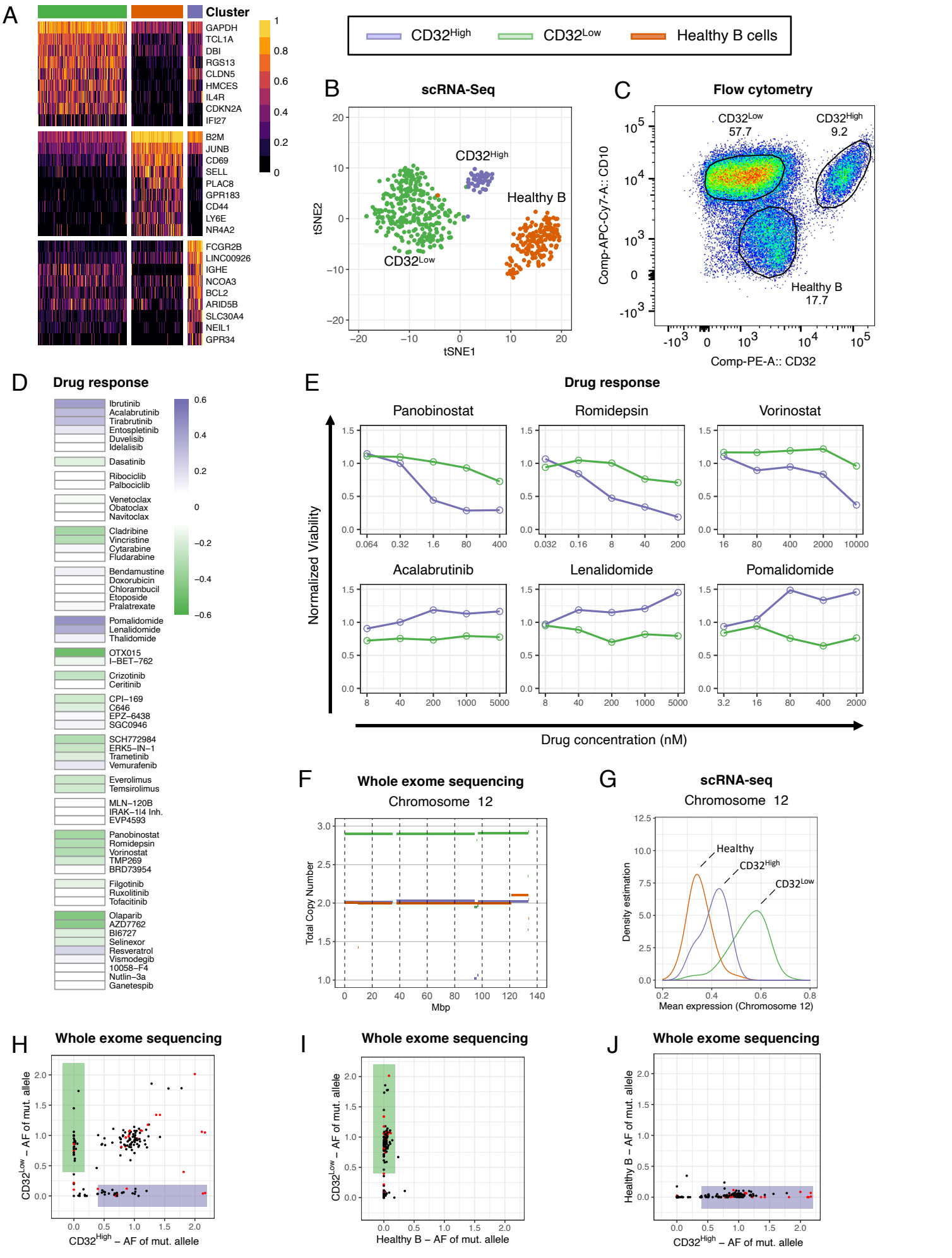
A
Cluster
GAPDH
TCL1A
DBI
RGS13
CLDN5
HMCES
IL4R
CDKN2A
IFI27
B2M
JUNB
CD69
SELL
PLAC8
GPR183
CD44
LY6E
NR4A2
FCGR2B
LINC00926
IGHE
NCOA3
BCL2
ARID5B
SLC30A4
NEIL1
GPR34
CD32High
CD32Low
Healthy B cells
B
scRNA-Seq
tSNE2
tSNE1
CD32High
Healthy B
CD32Low
C
Flow cytometry
CD32Low
57.7
CD32High
9.2
Healthy B
17.7
Comp-APC-Cy7-A:: CD10
Comp-PE-A:: CD32
D
Drug response
Ibrutinib
Acalabrutinib
Tirabrutinib
Entospletinib
Duvelisib
Idelalisib
Dasatinib
Ribociclib
Palbociclib
Venetoclax
Obatoclax
Navitoclax
Cladribine
Vincristine
Cytarabine
Fludarabine
Bendamustine
Doxorubicin
Chlorambucil
Etoposide
Pralatrexate
Pomalidomide
Lenalidomide
Thalidomide
OTX015
I–BET–762
Crizotinib
Ceritinib
CPI–169
C646
EPZ–6438
SGC0946
SCH772984
ERK5–IN–1
Trametinib
Vemurafenib
Everolimus
Temsirolimus
MLN–120B
IRAK–1I4 Inh.
EVP4593
Panobinostat
Romidepsin
Vorinostat
TMP269
BRD73954
Filgotinib
Ruxolitinib
Tofacitinib
Olaparib
AZD7762
BI6727
Selinexor
Resveratrol
Vismodegib
10058–F4
Nutlin–3a
Ganetespib
E
Drug response
Panobinostat
Romidepsin
Vorinostat
Acalabrutinib
Lenalidomide
Pomalidomide
Normalized Viability
Drug concentration (nM)
F
Whole exome sequencing
Chromosome 12
Total Copy Number
Mbp
G
scRNA-seq
Chromosome 12
Healthy
CD32High
CD32Low
Density estimation
Mean expression (Chromosome 12)
H
Whole exome sequencing
CD32Low – AF of mut. allele
CD32High – AF of mut. allele
I
Whole exome sequencing
CD32Low – AF of mut. allele
Healthy B – AF of mut. allele
J
Whole exome sequencing
Healthy B – AF of mut. allele
CD32High – AF of mut. allele

**Figure 5. In depth-analysis of sample tFL1**

A-B) Single cell RNA expression profiles of B cells derived from the tFL sample were subjected to SNN-based clustering. Three transcriptionally distinct clusters emerged. A) The heatmap illustrates the top 30 differentially expressed genes between all three identified clusters. Gene expression values were scaled to the maximum of each row. B) Clusters were colored and visualized in t-SNE projections of scRNA-seq expression profiles of malignant B cells. C) tFL1 derived lymph node cells were stained for viability, CD19, CD32, and CD10. The gates highlight three $CD19^{+}$ populations which correspond to the subclusters shown in panel B. D and E) Unsorted single cell suspensions from the tFL sample were incubated for 48 hours with 58 different drugs and five concentrations, and stained as described in panel C. Viability was normalized to vehicle control for each subpopulation separately. D) The mean difference of viabilities between the two malignant subclones is shown. White indicates that both malignant clones responded equally to this drug. Purple or green indicates that the viability of the $CD32^{High}$ or $CD32^{Low}$ subpopulation was superior. E) Six representative subclone specific responses to the following drugs are shown: panobinostat, vorinostat, romidepsin (HDAC inhibitors), acalabrutinib (BCR signaling inhibitor), lenalidomide and pomalidomide (immunomodulatory imide drugs). F) Whole exome sequencing was performed on FACS sorted $CD32^{High}$-, $CD32^{Low}$- and the non-malignant $CD10^{-}$ B cell subset. The line plot shows the total copy number estimation for chromosome 12 for all three sorted populations. The $CD32^{Low}$ clone harbors an additional copy of chromosome 12. G) Density curves of single cell expression values for all genes located on chromosome 12 are shown for each subclone. H-J) The scatter plots show the allele frequency (AF) of the mutated allele for exonic SNVs in both malignant subclones (H), in $CD32^{Low}$ versus healthy B cells (I) and in $CD32^{High}$ versus healthy B cells (J). Shaded purple or green boxes highlight SNV that are exclusive to one of the malignant B cell subclones. Red dots mark immunoglobulin-associated mutations. SNN: Shared-nearest-neighbor. HDAC: Histone deacetylase. BCR: B cell receptor. SNV: Single nucleotide variant.

# Figure 6

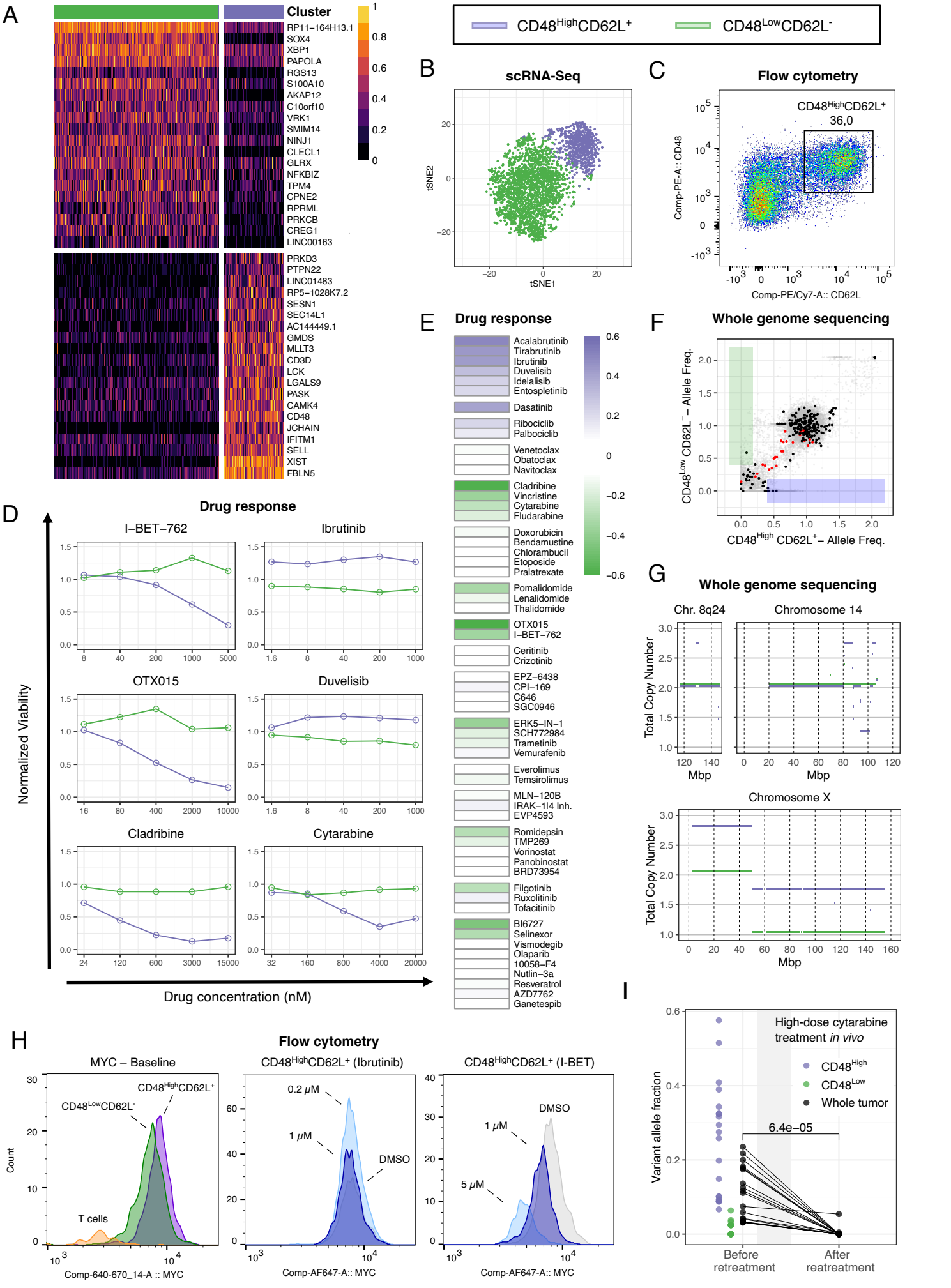
A
Cluster
RP11−164H13.1
SOX4
XBP1
PAPOLA
RGS13
S100A10
AKAP12
C10orf10
VRK1
SMIM14
NINJ1
CLECL1
GLRX
NFKBIZ
TPM4
CPNE2
RPRML
PRKCB
CREG1
LINC00163
PRKD3
PTPN22
LINC01483
RP5−1028K7.2
SESN1
SEC14L1
AC144449.1
GMDS
MLLT3
CD3D
LCK
LGALS9
PASK
CAMK4
CD48
JCHAIN
IFITM1
SELL
XIST
FBLN5
CD48HighCD62L+
CD48LowCD62L-
B
scRNA-Seq
tSNE1
tSNE2
C
Flow cytometry
CD48HighCD62L+
36,0
Comp-PE-A:: CD48
Comp-PE/Cy7-A:: CD62L
D
Drug response
I−BET−762
Ibrutinib
OTX015
Duvelisib
Cladribine
Cytarabine
Normalized Viability
Drug concentration (nM)
E
Drug response
Acalabrutinib
Tirabrutinib
Ibrutinib
Duvelisib
Idelalisib
Entospletinib
Dasatinib
Ribociclib
Palbociclib
Venetoclax
Obatoclax
Navitoclax
Cladribine
Vincristine
Cytarabine
Fludarabine
Doxorubicin
Bendamustine
Chlorambucil
Etoposide
Pralatrexate
Pomalidomide
Lenalidomide
Thalidomide
OTX015
I−BET−762
Ceritinib
Crizotinib
EPZ−6438
CPI−169
C646
SGC0946
ERK5−IN−1
SCH772984
Trametinib
Vemurafenib
Everolimus
Temsirolimus
MLN−120B
IRAK−1l4 Inh.
EVP4593
Romidepsin
TMP269
Vorinostat
Panobinostat
BRD73954
Filgotinib
Ruxolitinib
Tofacitinib
BI6727
Selinexor
Vismodegib
Olaparib
10058−F4
Nutlin−3a
Resveratrol
AZD7762
Ganetespib
F
Whole genome sequencing
CD48LowCD62L−− Allele Freq.
CD48High CD62L+− Allele Freq.
G
Whole genome sequencing
Chr. 8q24
Chromosome 14
Chromosome X
Total Copy Number
Mbp
H
Flow cytometry
MYC – Baseline
CD48HighCD62L+ (Ibrutinib)
CD48HighCD62L+ (I-BET)
CD48HighCD62L+
CD48LowCD62L-
T cells
0.2 μM
1 μM
DMSO
5 μM
Count
Comp-640-670_14-A :: MYC
Comp-AF647-A:: MYC
I
High-dose cytarabine treatment in vivo
CD48High
CD48Low
Whole tumor
6.4e−05
Variant allele fraction
Before retreatment
After reatreatment

**Figure 6. In depth-analysis of sample DLBCL1**

A-B) Single cell RNA expression profiles of malignant B cells derived from the DLBCL1 sample were subjected to SNN-based clustering. Two transcriptionally distinct clusters emerged. A) Top 40 differentially expressed genes between the two identified clusters are shown in the heatmap. Gene expression values were scaled to the maximum of each row. B) Clusters were colored and visualized in t-SNE projections of scRNA-seq expression profiles of malignant B cells. C) DLBCL1 derived lymph node cells were stained for viability, CD19, CD48 and CD62L (=SELL). The gate highlights a population which co-expresses CD62L and CD48, which represents the identified subclones. D and E) Lymph node derived cells from the DLBCL1 sample were incubated for 48 hours with 58 different drugs and 5 concentrations. Cells were stained as described in C. Viability was normalized to DMSO controls for each subpopulation separately. D) Six representative subclone-specific responses to the following drugs are shown: I-BET-762, OTX015 (BET inhibitors), ibrutinib, duvelisib (BCR signaling inhibitors), cytarabine and cladribine (chemotherapy). E) The mean difference of viabilities between the two subpopulations is shown. White indicates that both clusters responded equally to this drug. Purple or green indicates that the viability of the $CD48^{High}CD62L^{+}$ or $CD48^{Low}CD62L^{-}$ subpopulation was superior. F-G) Whole genome sequencing was performed on both FACS sorted populations ($CD48^{High}CD62L^{+}$, $CD48^{Low}CD62L^{-}$). F) The scatter plot shows the allele frequency (AF) of the mutated allele for non-synonymous exonic SNV in bold black and synonymous or intronic SNV in faded grey of both subclones. Shaded purple or green boxes highlight SNV that are exclusive to one or the other subclone. Red dots mark immunoglobulin-associated non-synonymous exonic mutations. G) Line plots show total copy number estimations for chromosome 8q24, 14 and X for both clones. H) DLBCL1 derived lymph node cells were incubated with DMSO control, I-BET-762 at two concentrations (1 µM, 5 µM) or ibrutinib at two concentrations (0.2 µM, 1 µM). At baseline and after 24 hours cells were harvested and stained for viability, CD19, CD3, CD48, CD62L and MYC or respective isotype control. Histograms show the fluorescence intensity of MYC at baseline for T cells, $CD48^{High}CD62L^{+}$ and $CD48^{Low}CD62L^{-}$ subclone, after 24 hours incubation with I-BET-762 and DMSO control or Ibrutinib and DMSO control. I) Shown are SNV with high variant allele frequencies in the $CD48^{High}CD62L^{+}$ subpopulation (purple) and low or undetectable in $CD48^{Low}CD62L^{-}$ subpopulation (green). Black circles show corresponding variant allele frequencies of whole tumor samples before and after retreatment with high-dose cytarabine. P value was calculated by the paired Wilcoxon-text. SNN: Shared-nearest-neighbor. BET: Bromodomain and Extra-Terminal motif protein. BCR: B cell receptor. SNV: Single nucleotide variant. DMSO: Dimethyl sulfoxide.